Supplementary Materials for
African smoke affects aerosol cycling over the Amazon

Bruna A. Holanda[1,2,a], Marco A. Franco[1,2], David Walter[1,3,c], Meinrat O. Andreae[4,5], Paulo Artaxo[2], Samara Carbone[6], Yafang Cheng[1], Sourangsu Chowdhury[7], Florian Ditas[1,a], Martin Gysel-Beer[8], Thomas Klimach[1], Leslie A. Kremper[1], Ovid O. Krüger[1], Jost V. Lavric[3,d], Jos Lelieveld[7], Chaoqun Ma[1], Luiz A. T. Machado[1,2], Fernando G. Morais[2], Robin L. Modini[8], Andrea Pozzer[7], Jorge Saturno[1,b], Hang Su[1], Manfred Wendisch[9], Stefan Wolff[1], Mira L. Pöhlker[1,9,10], Ulrich Pöschl[1], and Christopher Pöhlker[1,4,*]

[1]Multiphase Chemistry Department, Max Planck Institute for Chemistry, 55128 Mainz, Germany

[2]Institute of Physics, University of São Paulo, São Paulo 05508-900, Brazil

[3]Department of Biogeochemical Processes, Max Planck Institute for Biogeochemistry, 07701 Jena, Germany

[4]Biogeochemistry Department, Max Planck Institute for Chemistry, 55128 Mainz, Germany

[5]Scripps Institution of Oceanography, University of California San Diego, La Jolla, CA 92037, USA

[6]Federal University of Uberlândia, Uberlândia-MG, 38408-100, Brazil

[7]Atmospheric Chemistry Department, Max Planck Institute for Chemistry, 55128 Mainz, Germany

[8]Laboratory of Atmospheric Chemistry, Paul Scherrer Institute, 5232 Villigen PSI, Switzerland

[9]Leipzig Institute for Meteorology, Leipzig University, Leipzig, Germany

[10]Experimental Aerosol and Cloud Microphysics Department, Leibniz Institute for Tropospheric Research, Leipzig, Germany

[a]now at: Hessian Agency for Nature Conservation, Environment and Geology, 65203 Wiesbaden, Germany

[b]now at: Physikalisch-Technische Bundesanstalt, 38116 Braunschweig, Germany

[c]now at: Climate Geochemistry Department, Max Planck Institute for Chemistry, 55128 Mainz, Germany

[d]now at: Acoem Ecotech, 1492 Ferntree Gully Road, Knoxfield VIC 3180, Melbourne, Australia

[*]Corresponding author: C. Pöhlker. E-mail: c.pohlker@mpic.de

This manuscript was compiled on April 1, 2023

Contents

1 Supplementary Notes: Biomass burning aerosol source assignment

Previous studies indicated – and the present study strongly supports – that the biomass burning smoke in the Amazon can be regarded as a mixture of South American and African fires with a high spatiotemporal variability of both influences [e.g., 1–6]. Related to the approach by Liu *et al.* [7], we used differences in the rBC microphysical properties for a source assignment of the biomass burning smoke over the Amazon Basin. We analyzed two full seasonal cycles of rBC data measured at ATTO in combination with several satellite products and backward trajectory analysis (Supplementary Figure 3). The carbon monoxide concentrations over the ocean just before reaching the coast (CO_{ROI}, Supplementary Figure 3A, Sect. 4.5) and the cumulative fire count along the backward trajectories (BT) in the ATTO footprint (CF_{BT}, Supplementary Figure 3B, Sect. 4.6), are used as proxy for African smoke influx into the Amazon and for periods with intense South American smoke influence, respectively. The cumulative precipitation along the 3-day BTs (P_{BT}, Supplementary Figure 3C, Sect. 4.7) represents the aerosol wet scavenging in air masses arriving at ATTO. The overall ATTO time series of the rBC mass concentration (M_{rBC}) and size distribution – specifically the geometric mean diameters (D_{rBC}) and geometric standard deviation (σ_{rBC}) retrieved from a systematic monomodal fitting of 3-h averaged rBC mass size distributions – are shown in (Supplementary Figure 3D–F). We observed a pronounced seasonality and high variability in D_{rBC} and σ_{rBC}, which we hypothesize to be modulated by the relative contributions of sources. To verify that, we identified a certain number of 'event periods' with dominant advection of either African or South American smoke (color shading in Supplementary Figure 3) in order to obtain their characteristic rBC mass size distributions.

1.1 Determination of characteristic rBC mass size distribution

Periods with mostly South American smoke at ATTO spanned from 06 to 11 August 2019 and from 28 July to 11 August 2020 with elevated rBC mass concentrations (green shading in Supplementary Figure 3). In these periods, CO_{ROI}, was at a minimum, suggesting low advection of African smoke at the same time that a maximum in CF_{BT} was observed. On the other hand, characteristic episodes of mostly African smoke at ATTO with M_{rBC} exceeding $1\,\mu g\,m^{-3}$ occurred from 20 to 23 January and 03 to 09 February 2020 (gray shading in Supplementary Figure 3). These events belong to the early Amazonian wet season, when fire occurrence in the Amazon, and specifically along the ATTO BT footprint, approaches its minimum due to frequent and intense rainfall and efficient aerosol scavenging (see Supplementary Figure 3 B and C). Accordingly, an influence from

South American fires can be largely neglected, as shown in previous studies [e.g., 2, 5, 8, 9]. The high M_{rBC} can be therefore explained by long-range transport of African aerosol plumes, which bring a mixture of dust and smoke and occurs prominently between December and April as outlined in detail in Moran-Zuloaga *et al.* [2]. Note that the high rBC concentrations at ATTO related to the BB pollution occur during the 'rain windows', when the P_{BT} in Supplementary Figure 3 C is at minimum.

To illustrate the contrasting atmospheric conditions, Figs. 2A and 2B show daily composite maps with satellite images, fire maps, wind fields, and backward trajectories for exemplary days with a preponderance of either African or South American BB influence. Figure 2A shows an example of southerly winds transporting dense smoke from fire hotspots along the large highways BR-230 and BR-163 into the central basin on 06 August 2019. The heavy smoke could visually be traced from the fires to ATTO in satellite images. Further, the influence of African BB was low during this episode since the long-range transport from Africa is associated with easterly rather than southerly advections. In contrast, Fig. 2B shows strong winds and rather 'straight' northeasterly backward trajectories without noticeable fire contact over South America. This corresponds to the typical air mass advection patterns of long-range transport of African aerosols [see 2]. Further, Fig. 2C and Fig. 2D show that in spite of intense burning activities in the Amazon Basin, predominant easterly winds bring a mixture of South American and African biomass burning smoke to the ATTO site.

The statistical analyses of D_{rBC} and the σ_{rBC} for the 'event periods' with dominant African or South American BB influences are shown in Supplementary Figure 4A and Supplementary Table 1 and highlight the significant differences in the rBC properties between both smoke types. We found that smoke from South American fires – which refers especially to fires in the ATTO footprint region as shown in Pöhlker *et al.* [8] – is characterized by comparatively small rBC cores (i.e., $176 < D_{\mathrm{rBC}} < 185\,\mu\mathrm{m}$) as well as broad rBC core size distribution (i.e., $1.64 < \sigma_{\mathrm{rBC}} < 1.69$). In contrast, the aged smoke from African fires after transatlantic transport is characterized by comparatively large rBC cores (i.e., $215 < D_{\mathrm{rBC}} < 219\,\mu\mathrm{m}$) and narrow rBC core size distribution ($1.47 < \sigma_{\mathrm{rBC}} < 1.49$). These differences in D_{rBC} and σ_{rBC} appear to be remarkably robust throughout the 2–year time series analyzed here.

Further, the characteristic rBC distributions for biomass burning plumes at ATTO were compared with two complementary aircraft campaigns over the Amazon (ACRIDICON-CHUVA) and over the Atlantic Ocean (CAFE-Africa) (see Sect. 4.2). During ACRIDICON-CHUVA, two distinctly different conditions were probed: First, four fresh biomass burning plumes were probed directly over fires in the Amazon, which therefore represent reference cases for pure and fresh Amazonian smoke. For these plumes, averages of $D_{\mathrm{rBC,AC,SAm}} = 180 \pm 8\,\mathrm{nm}$ and $\sigma_{\mathrm{rBC,AC,SAm}} = 1.59 \pm 0.03$ were obtained. Second, defined pollution layer(s) at $\sim$3.5 km altitude, in which smoke from southern Africa was transported across the Atlantic, were analyzed as outlined in Holanda *et al.* [4]. Under these conditions pure African smoke after $10 - 15$ days of transport was probed over and off the Brazilian coast in stable atmospheric layers, prior to being mixed into the convective boundary layer over the Amazon. In this layer, we found averages of $D_{\mathrm{rBC,AC,Afr}} = 202 \pm 8\,\mathrm{nm}$ and $\sigma_{\mathrm{rBC,AC,Af}} = 1.49 \pm 0.04$. During CAFE-Africa, the transatlantic transport of African smoke was sampled intensively at different locations over the Atlantic Ocean (Fig. 1A$_2$) and, therefore, at different aging times, yielding an average of $D_{\mathrm{rBC,CA,Afr}} = 226 \pm 8\,\mathrm{nm}$ and $\sigma_{\mathrm{rBC,CA,Afr}} = 1.49 \pm 0.04$. A small variability within the different flights was observed, which can possibly be attributed to different source regions in Africa. Nevertheless, all independent flight measurements during CAFE-Africa are statistically comparable, indicating rather stable rBC mass size distributions during transatlantic transport.

Supplementary Figure 4 and Table 1 summarize the statistics of D_{rBC} and σ_{rBC} for all ground-based and aircraft campaigns addressed in this study as well as further aircraft campaign in literature. The D_{rBC} and σ_{rBC} from the aircraft and ATTO data agree remarkably well, suggesting that the smoke from African and South American fires can be represented by generalized rBC signatures.

1.2 Different rBC properties observed at ATTO

Previous studies indicated that differences in the rBC size distributions can be related either to differences in the combustion and emission process, which includes fuel types, fuel moisture content, and flaming vs smoldering conditions, or to differences in atmospheric transport and aging, which can be driven by coagulation or size-dependent particle removal through rain-out [e.g., 10–15]. Our measurements don't allow to draw conclusions on the reasons for the distinct rBC mass size distributions between regional and distant (transcontinental) sources observed over the Amazon. However, below, we summarize the observations suggesting that the contrasting rBC properties (i.e., D_{rBC} and σ_{rBC}) are robust and can represent a general rBC signature for the African and South American smoke over the Amazon region:

1. **BC-BC coagulation:** The rBC mass size distribution of African smoke measured at ATTO agrees well with our aircraft measurements at different locations of the Atlantic Ocean closer to the African coast and therefore, at different aging times, measured during the CAFE-Africa campaign (see Sect. 4.2). This suggests that horizontal transport at high altitudes over the Atlantic Ocean, or downwards into the continental boundary layer, does not change the rBC signature to a significant extent. In fact, on the way to South America, the African smoke travels typically more than 10 days within highly stratified aerosol layers up to 5.5 km height over the Atlantic Ocean [2–4, 16, 17]. Over the ocean, the number concentration of rBC particles in these smoke layers are too low ($\sim$ 100's cm^{-3}) for self-coagulation to be an important process on these timescales [18, 19]. Also in measurements closer to the source, when particle concentrations are orders of magnitude higher, no significant increase in D_{rBC} due to BC-BC coagulation was observed [20, 21].

2. **Size selection due to wet scavenging:** In addition, we consider that the African smoke did not undergo relevant wet scavenging neither during horizontal transport over the Atlantic nor over the South American continent prior to reaching the ATTO site, which could influence the rBC mode diameter [10]. Over the Atlantic, the atmospheric circulation follows the St. Helena high pressure system, and, therefore, African smoke encounters few precipitating clouds during transatlantic transport. When the smoke layers of African smoke are advected over the South American continent, where convection sets in, large scale subsidence or downdrafts from convection distributes the African aerosol vertically into the continental boundary layer, which is responsible for elevating the BC concentrations at the ATTO site. Still, no noticeable size selection due to rain-out on the way from the offshore region to the ATTO site is observed, as suggested by the cumulative rain along the BTs (Fig. 1B$_3$). For the South American smoke, the transport time of the smoke from fires in the footprint region to ATTO is between 1 to 4 days and the smoke is transported horizontally within a well mixed layer up to 3.5 km altitude [see Supplementary Figure 12 and 17]. Due to the good agreement between our measurements at ATTO (within the boundary layer in central Amazon) and aircraft measurements (higher altitudes and closer to the sources), we assume that no size selection due to rain-out occurs during horizontal transport over South America.

3. **Fuel mix:** The fuel mixture in the ATTO BT footprint region on the South American continent differs clearly from the African fuel mixture (compare Supplementary Figure 8 and Supplementary Figure 9). In South America, fires in evergreen rain forest regions in the Amazonia ecosystem followed by fires in the Cerrado (savanna) are the most relevant for ATTO. In addition, sensitivity model runs taking into account fire emissions over the different Brazilian ecosystems show that Amazonia and Cerrado are the dominant source ecosystems for the South American biomass burning smoke (including both local and regional sources) arriving at the ATTO site, depending on the time of the year (**??**). Although biomass burning is the dominant source of BC particles at ATTO, causing the sharp peaks in BC concentrations, Supplementary Figure 6 also indicates that some background pollution from anthropogenic sources may play a role in the rBC size distributions – however in much lower relative concentrations. On the other hand, fires in Africa comprise mostly dry vegetation (i.e., deciduous open and closed forests, shrublands,

and herbaceous landscapes) and suggest a dominance of a flaming fire regime [22]. In addition, we
found similar average fuel mixtures in Northern and Southern Africa (Supplementary Figure 9 C_2 and
D_2). Accordingly, a consistent rBC signature was obtained for smoke from Northern Africa, measured at
ATTO in the wet season, and Southern Africa, measured by the aircraft in the dry season (Supplementary
Figure 4).

4. **Fuel mix in South America:** Differences in rBC mass size distributions emitted from the different
   vegetation fires in South America were investigated during the SAMBBA campaign over the Amazon
   Basin in the dry season of 2012 [23]. Supplementary Figure 4D shows the D_{rBC} and σ_{rBC}, respectively,
   obtained from several aircraft transects within smoke from active fires over the Amazonia and Cerrado
   vegetation. A small difference in the core diameters between the two main types of vegetation burnt in
   the ATTO footprint was observed, however this difference is not as significant as that one related to the
   long-range-transported African smoke. Also note the good agreement between D_{rBC} between SAMBBA
   and the ATTO and ACRIDICON measurements. The σ_{rBC} in both Amazonia and Cerrado vegetation is,
   however, more narrow compared to our observations, which can be explained by the negligible influence
   of additional sources during the SAMBBA flights. It should be taken into account that the SAMBBA
   measurements were taken much closer to the sources compared to our measurements at ATTO or during
   ACRIDICON-CHUVA, where smoke from different vegetation types or some additional pollution may
   be mixed into in the BB smoke, leading to a broader size distribution (as suggested in Supplementary
   Figure 6 and **??**). Therefore the term 'South American smoke' is a good approximation for the mixture
   between the fires over the different ecoregions in the ATTO footprint, agricultural fires, and the continental
   urban background.

5. **Plume lifting over Africa:** Plume lifting to high altitudes during convective updrafts and cloud pro-
   cessing over Africa could lead to even larger BC cores in African plumes in addition to the vegetation
   type. However, observations of rBC properties over Africa are still sparse. Recently, as part of the MOYA
   campaign over Western Africa in the wet season, Wu *et al.* [20] reported D_{rBC} of 181-207 nm in fresh
   and slightly aged biomass burning plumes. Also Taylor *et al.* [21] reported an increase in D_{rBC} at higher
   altitudes over the South Atlantic Ocean. However, further research over the African continent is needed
   to address this question.

1.3 Bimodal fitting – the deconvolution method

Given that South American vs African smoke is characterized by robust differences in rBC properties, we
propose deconvoluting quantitatively the rBC mass size distributions time series at ATTO as a superposition
of both smoke types. Therefore, we conducted a systematic bimodal fitting to every 3-h averaged rBC mass
size distribution constrained to the characteristic size distributions of the African and South American rBC
cores. The fit was applied across the rBC size range from 90 to 500 nm. The following function according to
Heintzenberg [24] was used

$$f(d_{\mathrm{MEV}}) = \frac{A_{\mathrm{rBC,SAm}}}{\sqrt{2\pi}log(\sigma_{\mathrm{rBC,SAm}})} \exp\left[-\frac{(log(d_{\mathrm{MEV}}) - logD_{\mathrm{rBC,SAm}})^2}{2log^2(\sigma_{\mathrm{rBC,SAm}})}\right] + \frac{A_{\mathrm{rBC,Afr}}}{\sqrt{2\pi}log(\sigma_{\mathrm{rBC,Afr}})} \exp\left[-\frac{(log(d_{\mathrm{MEV}}) - logD_{\mathrm{rBC,Afr}})^2}{2log^2(\sigma_{\mathrm{rBC,Afr}})}\right]$$

(S1)

with the fit parameters $D_{rBC,i}$ as geometric mean diameter, $\sigma_{rBC,i}$ as geometric standard deviation, and $A_{rBC,i}$
as the rBC mass concentration at $D_{rBC,i}$. The bimodal fit comprised one 'African (Afr) mode' and one 'South
American (SAm) mode'. The fit parameters $D_{rBC,i}$ and $\sigma_{rBC,i}$ were constrained according to the rBC properties
for nearly 'pure' African and South American smoke (Supplementary Figure 4). Specifically, the following
constraints were used for the African mode:

- $A_{\text{rBC,Afr}}$ was a free parameter

- $D_{\text{rBC,Afr}}$ was constrained within the range from 215 to 219 nm

- $\sigma_{\text{rBC,Afr}}$ was constrained within the range from 1.47 to 1.49

The following constraints were used for the South American mode:

- $A_{\text{rBC,SAm}}$ was a free parameter

- $D_{\text{rBC,SAm}}$ was constrained within the range from 176 to 185 nm

- $\sigma_{\text{rBC,SAm}}$ was constrained within the range from 1.64 to 1.69

For illustration, examples of individual bimodal fits are shown in Supplementary Figure 5.

Based on the bimodal fits, the African ($M_{\text{rBC,Afr}}$) vs South American ($M_{\text{rBC,SAm}}$) contributions to the total M_{rBC} were quantified as the integral mass concentrations of rBC cores of the corresponding modes over the full size range. This include potential tails outside the SP2 detection range, however, this represents only a small contribution. Only successful fits ($R^2 > 0.95$) were considered for further analysis. The resulting time series of the separated influence of African vs South American rBC based on this approach, which we refer to as the deconvolution method, is shown in Fig. 3.

Note that the number of modes (n) fitted in Eq. S1 can be in principle as high as the number of different combustion sources, given that they are characterized by different microphysical rBC properties. By applying the bimodal fit, we assume that biomass burning in Africa and in South America are the only two sources providing BC particles to the ATTO site. This assumes that other potential emission sources, such as urban pollution (for example from Manaus city, see Martin *et al.* [25] and Martin *et al.* [26]), do not significantly contribute to rBC mass concentration at ATTO, which is justified according to Pöhlker *et al.* [8] and model simulations in Supplementary Figure 6.

Based on the relative contribution of South America and African smoke, the aerosol properties at ATTO were classified into the following five pollution regimes:

- **Dominant South American influence**: $M_{\text{rBC,SAm}}/M_{\text{rBC}} > 0.80$

- **Majoritarian South American influence**: $0.5 < M_{\text{rBC,SAm}}/M_{\text{rBC}} < 0.80$

- **Majoritarian African influence**: $0.5 < M_{\text{rBC,Afr}}/M_{\text{rBC}} < 0.80$

- **Dominant African influence**: $M_{\text{rBC,Afr}}/M_{\text{rBC}} > 0.80$

- **Pristine**: $M_{\text{rBC}} < 0.01 \, \mu\text{g m}^{-3}$ according to the definition in Pöhlker *et al.* [27]

Figure 3C shows the classification flag for pollution regimes, which were the basis for the determination of several climate relevant physico-chemical and optical parameters within the two dominant smoke types at the ATTO site. A statistical analysis of several aerosol properties is presented in the next section (Supplementary Notes 1.4).

1.4 Physico-chemical properties of South American and African smoke

Generally, open vegetation fires always combine flaming and smoldering combustion, while the relative contributions of both are highly variable and strongly depend on fuel and environmental conditions [22, 28–32]. The carbon monoxide (CO) concentration and especially the enhancement ratio between BC and CO (ΔBC/ΔCO) are established markers for the extent of smoldering involved. Here, we found comparatively high values of ΔBC/ΔCO $= 23.7 \pm 4.0 \, \text{ng m}^{-3}\text{ppb}^{-1}$ (Supplementary Figure 13A) for the African-dominated smoke, suggesting mostly flaming combustion, which is in line with the relatively dry vegetation mixture at the fire locations

in Africa (see Supplementary Figure 9). In contrast, rather low values of $\Delta BC/\Delta CO = 4.5 \pm 0.2\,\mathrm{ng\,m^{-3}ppb^{-1}}$ were observed for the South American-dominated smoke, suggesting a more smoldering combustion, which is consistent with the rather moist fuel in the ATTO footprint region (Supplementary Figure 8).

The African smoke contributes significantly to the BC burden over the Amazon while contributing to a lesser extent to the aerosol number concentrations. The fact that African smoke is much richer in rBC relative to non-absorbing material is reflected in the rBC mass and number fractions (Supplementary Figure 13B), which is significantly higher for African than for South American-dominant episodes. Moreover, we calculate that the number of $CCN_{0.3}$ produced per mass of rBC is $1.8 \cdot 10^9\,\mu\mathrm{g}^{-1}$ in South American dominant conditions, while it is 10 times lower in African-dominant condition (Supplementary Figure 13C–D). The enriched BC in African fires are related, among other factors, to more flaming combustion — i.e., the BC emissions are proportionally higher already at the sources (see Wu *et al.* [20]) –, and tends to further increase during the transatlantic transport due to the loss of organics by photo-bleaching.

The level of chemical oxidation of the organic aerosol can be inferred from key organic fragments (m/z 43, 44) presented in Supplementary Figure 14. These results suggest that African smoke is more oxidized as it shows the highest f44 signals (corresponding mostly to the fragment CO_2^+) at the same time that the f43 signals (most likely related to the fragment $C_2H_3O^+$) are the lowest. Further, the main levoglucosan fragment $f60$ (mostly ions $C_2H_4O^+$), often used as a marker for biomass burning [33], quickly degrades in the atmosphere within the first few hours after emission. In all biomass burning regimes at ATTO, f60 lies close to the reference value of 0.3 ± 0.06 for negligible or completely oxidized biomass-burning PM1 [33], meaning that all BB plumes probed at ATTO have aged for at least 9 –12 h in the atmosphere before reaching the remote ATTO site (see the $f60$ decay curve in Wu *et al.* [20]). Our results from ATTO are consistent with chemical composition data from previous studies over the Amazon Basin [34–37] and in African plumes over the South Atlantic [e.g. 20, 21].

The shapes of the normalized particle number size distribution (PNSD) for the 5 atmospheric regimes are shown in Supplementary Figure 15. For the South American dominant regime, a bimodal PNSD is observed at ATTO, with a pronounced mode in the accumulation size range peaking at $D_{\mathrm{acc,SAm}} = 153.4\,(0.63)\,\mathrm{nm}$ (geometric mean diameter and geometric standard deviation) and engulfing a less pronounced Aitken mode at $D_{\mathrm{ait,SAm}} = 72\,(0.64)\,\mathrm{nm}$. The PNSD shape for the African dominant state presents a more defined bimodal shape, with the accumulation mode peaking at larger diameters, $D_{\mathrm{acc,Afr}} = 196.4\,(0.92)\,\mathrm{nm}$, and an Aitken mode peaking at $D_{\mathrm{ait,Afr}} = 75\,(1.05)\,\mathrm{nm}$. The PNSD for the pristine regime is substantially different from the biomass burning dominated states, presenting a pronounced Aitken mode at $D_{\mathrm{ait,pri}} = 70.7\,(0.37)\,\mathrm{nm}$ and engulfing an accumulation mode at $D_{\mathrm{acc,pri}} = 174.8\,(1.01)\,\mathrm{nm}$. Overall, the shapes of the PNSDs derived for the pristine, African-dominant and South American-dominant regimes in this study are in remarkable agreement with the 'pristine', 'long-range-transport' and 'biomass burning' case studies analyzed in Pöhlker *et al.* [27], respectively. Therefore, the African smoke contributes a small number of CCN with high hygroscopicity to the Amazon Basin, whereas the fires in South America contribute significantly to the CCN number, but are less hygroscopic. The net effect of aerosol-radiation and aerosol-cloud interactions over the Amazon Basin needs to be investigated.

The higher SSA for the South American relative to the African smoke corresponds to a lower f_{rBC} and, thus larger fraction of non-absorbing particles (Supplementary Figure 16A). The lower SSA for African smoke was observed across the entire wavelength range analyzed here, which shows a quasi-linear decrease in SSA towards higher wavelengths (Supplementary Figure 16B), in agreement with previous studies [38–40].

1.5   Observation-model comparison

Beyond the comparison with two global models in Fig. 5 and Supplementary Figure 18, the experimental rBC mass concentrations at ATTO were also compared to the corresponding BC concentration output of the MERRA-2 reanalysis data (Supplementary Figure 19). Note that only the total BC at ATTO was derived from

MERRA-2. Only a moderate agreement was obtained between the total measured rBC and the MERRA-2 data, with $R = 0.60$ (Supplementary Figure 19A and C). Remarkably, the comparison of the MERRA-2 output and the rBC concentration from South American fires obtained from the deconvolution method yielded a much better agreement with $R = 0.80$ (Supplementary Figure 19B and D). While the modelled rBC concentrations are still a factor 2 higher than the observed values, the temporal variability is captured remarkably well. This suggests that MERRA-2 represents the South American BC sources well (with a constant factor), but at the same time underestimates the African emissions grossly. Again, the good agreement in Supplementary Figure 19B underlines the robustness of the classification method based on microphysical rBC properties presented in Supplementary Notes 1.3.

2 Supplementary Tables

Supplementary Table 1: Statistical analysis of the fit parameters obtained by applying a monomodal fit to the individual BC mass size distributions. The ATTO size distributions was averaged to 3-h and the HALO data to 10 seconds prior to applying the fitting.

|		ATTO periods		ACRIDICON-CHUVA		CAFE-Africa						SAMBBA	
		SAm	Afr	Amz	Afr LRT	all	CA04	CA05	CA12	CA13	CA15	Amz	Cerrado
D_{rBC}	Avg	181	217	180	202	226	225	227	219	231	221	179	192
	Std	3	2	8	8	8	5	5	7	8	9	4	9
	P09	176	215	173	193	217	220	221	214	219	214	174	185
	P25	179	216	176	197	221	222	223	217	224	217	177	189
	P50	181	217	180	201	225	225	226	219	232	219	179	192
	P75	183	218	184	206	230	227	229	222	237	223	181	195
	P91	185	219	190	214	237	229	234	225	240	227	184	199
σ_{rBC}	Avg	1.66	1.48	1.59	1.49	1.49	1.50	1.49	1.51	1.48	1.50	1.49	1.52
	Std	0.02	0.01	0.03	0.04	0.04	0.03	0.03	0.04	0.03	0.04	0.03	0.04
	P09	1.64	1.47	1.56	1.44	1.45	1.48	1.45	1.48	1.44	1.46	1.45	1.49
	P25	1.65	1.47	1.57	1.46	1.48	1.49	1.47	1.50	1.46	1.48	1.47	1.50
	P50	1.66	1.48	1.59	1.48	1.49	1.50	1.49	1.52	1.48	1.50	1.49	1.52
	P75	1.67	1.48	1.60	1.51	1.51	1.51	1.51	1.53	1.50	1.52	1.51	1.54
	P91	1.69	1.49	1.62	1.54	1.53	1.52	1.53	1.55	1.52	1.55	1.53	1.56
	N	126	92	13	297	1968	516	310	262	630	250	153	814

3 Supplementary Figures
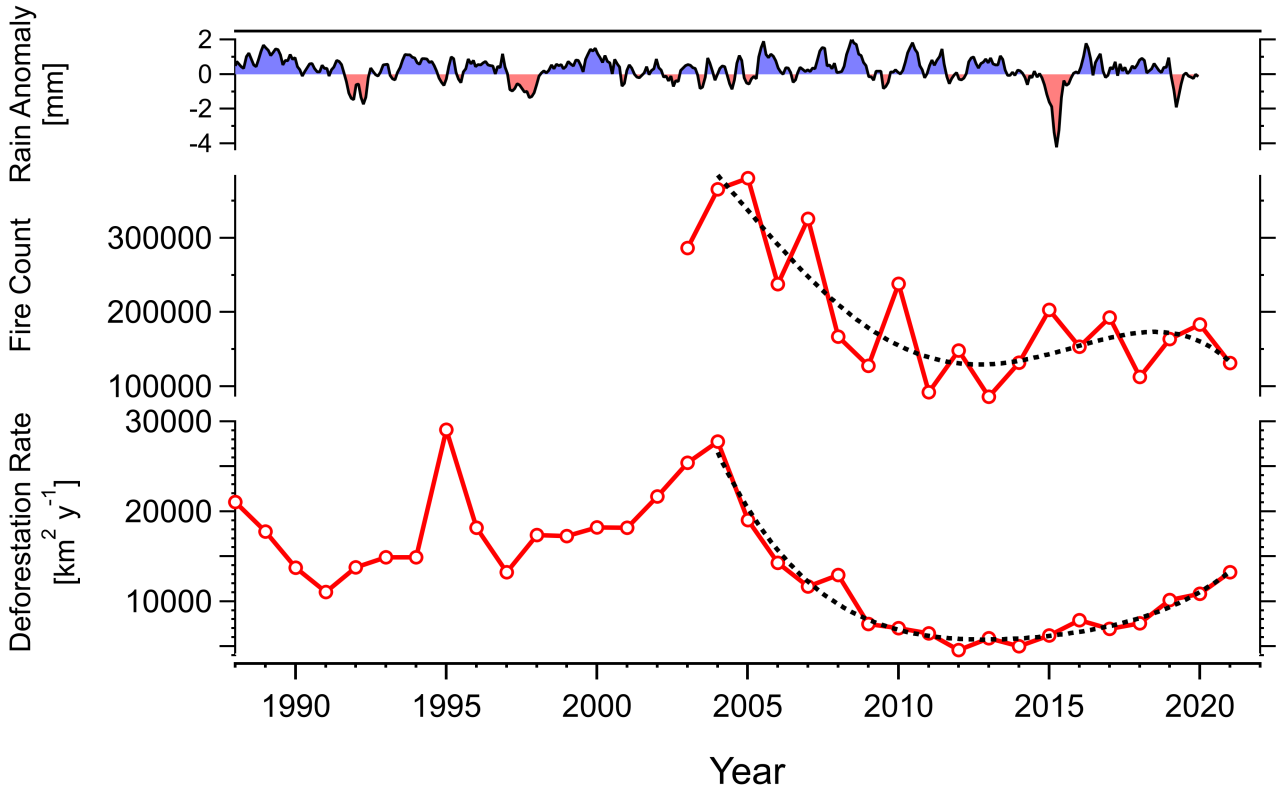
Supplementary Figure 1: Annual rainfall anomaly **(A)**, annual fire count **(B)**, and annual deforestation rate **(C)** in the Brazilian Amazon. The fire count since 2003 was obtained from the satellites Terra and Aqua via https://queimadas.dgi.inpe.br/queimadas (last access, 18 Feb 2022). Deforestation rates since 1988 were obtained from http://www.obt.inpe.br/OBT/assuntos/programas/amazonia/prodes (last access, 18 Feb 2022). The rainfall anomaly was calculated as outlined in Pöhlker *et al.* [8]. Fire counts and deforestation rates starting at the historic deforestation peak in 2004 [41] were fitted with the polynomial function $y = K_0 + K_1(x - 2004) + K_2(x - 2004)^2 + K_3(x - 2004)^3 + K_4(x - 2004)^4$ to emphasize the overall trend, with the fit parameters (i) $K_0 = 26555$, $K_1 = -7014$, $K_2 = 883$, $K_3 = -51$, $K_4 = 1214$ for the deforestation rate and (ii) $K_0 = 26555$, $K_1 = -7014$, $K_2 = 883$, $K_3 = -51$, $K_4 = 1214$ for the fire count.
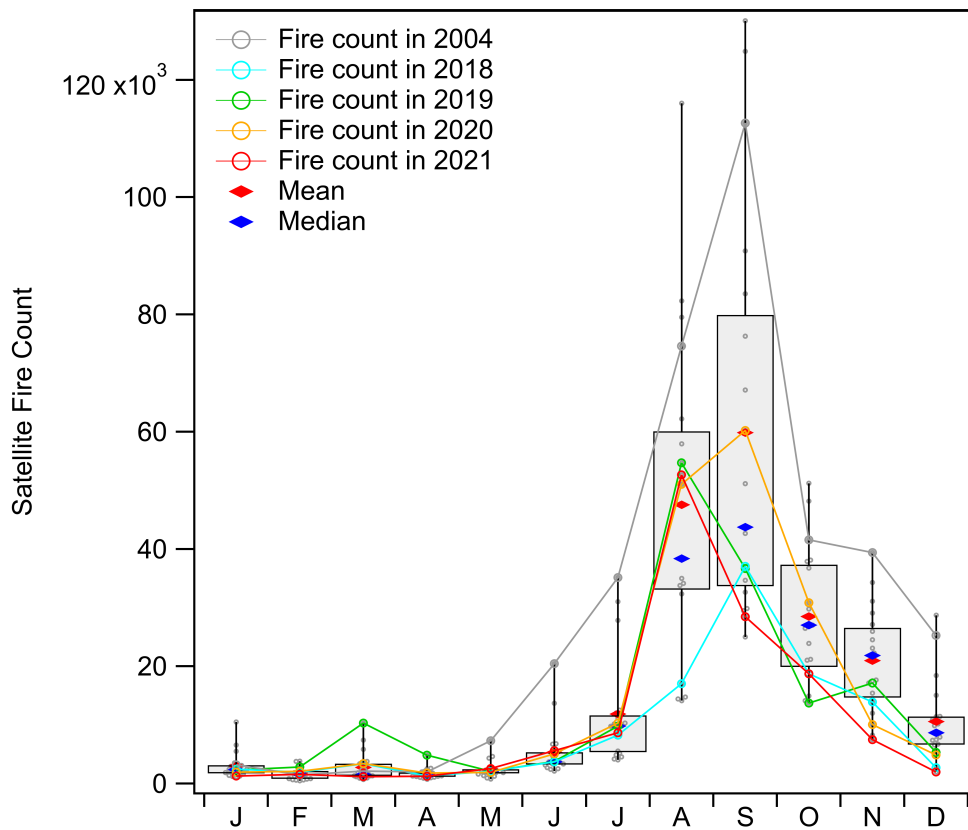
Supplementary Figure 2: Increase of detected fires in recent years in Amazonia, emphasized by Box-Whisker plots of the seasonal cycle in number of satellite-detected fires for two time frames: **(A)** from 2003-01-01 to 2021-08-31 and **(B)** from 2010-01-01 to 2021-12-31. The fire counts were derived from Brazilian National Institute for Space Research data (Instituto Nacional de Pesquisas Espaciais, INPE, http://queimadas.dgi.inpe.br/queimadas/bdqueimadas, last access 28 July 2021). From all satellites used in the INPE data, only the NASA satellites Terra and Aqua were used here because both span the longest continuous time period and allowed calculating multi-year anomalies. The boxes specify the interquartile range with the median as blue diamond marker and the mean as red diamond marker. The whiskers specify the minimum and maximum values. Fire counts of individual years are highlighted as colored open circular markers: (i) 2004 as one of the years with strongest fire activity, also corresponding to peaking deforestation rates in the Amazon [41]; (ii) 2018 as a year with comparatively low fire activities; (iii) 2019 and 2020 as the years of interest of the present study, which both show significant increases in fire counts relative to the previous years; (iv) 2021 showing the most recent situation.
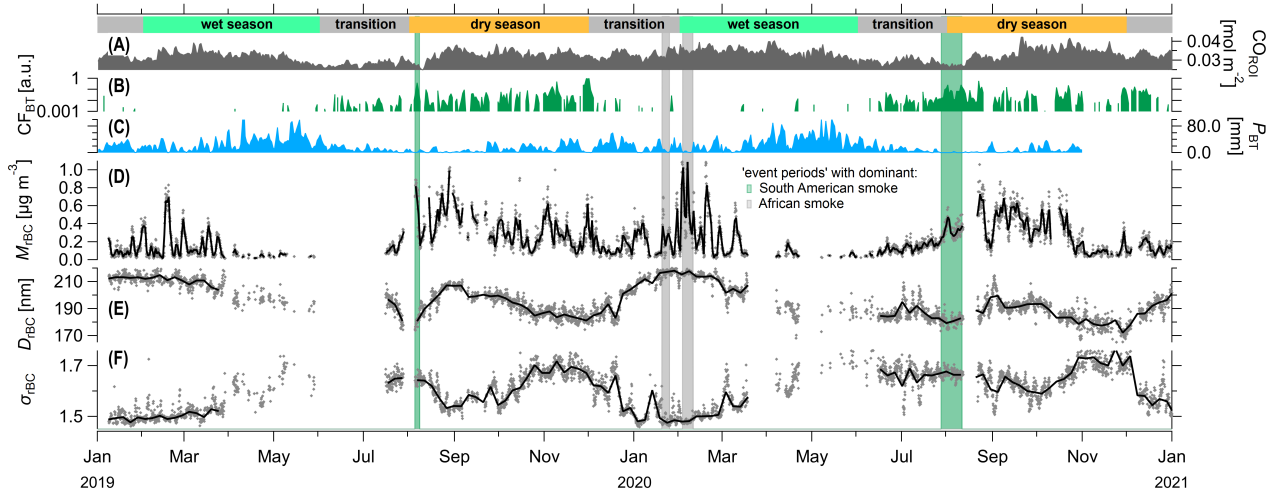
Supplementary Figure 3: **(A)** As proxy for African smoke influx into the Amazon: satellite-derived CO concentration in the offshore region of interest off the Brazilian coast ($ROI_{offshore}$, Sect. 4.5). **(B)** As proxy for periods with intense South American smoke influence: cumulative number of fires, CF_{BT}, along the 3-day BTs starting at 200 m at ATTO according to [4]. **(C)** As proxy for aerosol wet scavenging in air masses arriving at ATTO: cumulative precipitation, P_{BT}, along the 3-day BTs according to [8]. **(D − F)** Time series of rBC mass concentration, M_{rBC}, geometric mean diameter, D_{rBC}, and geometric standard deviation, σ_{rBC}, derived from monomodal fitting of 3 h averaged rBC mass size distributions. Green and gray vertical shadings indicate ATTO 'event periods' with dominant influence of South American (i.e., 28 Jul – 11 Aug 2020) vs African smoke (i.e., 20 – 23 Jan and 03 – 09 Feb 2020).
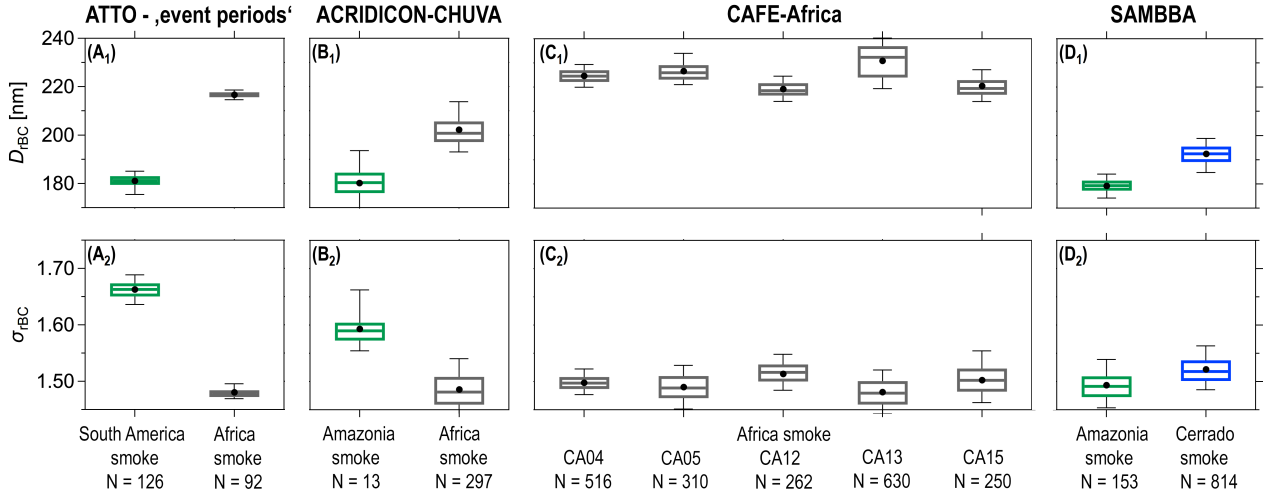
Supplementary Figure 4: Statistics of the fit parameters, geometric mean diameter (D_{rBC}) and geometric standard deviation (σ_{rBC}), from fitted rBC mass size distributions during characteristic conditions of ATTO and aircraft measurements, emphasizing the clear differences in rBC microphysical properties between African and South American smoke. ($\mathbf{A_1}$ and $\mathbf{A_2}$) ATTO 'event periods' as highlighted in Supplementary Figure 3. ($\mathbf{B_1}$ and $\mathbf{B_2}$) Smoke conditions during ACRIDICON-CHUVA [42] – specifically a layer of long-range transported African smoke – as well as fresh Amazonian fires plumes as analyzed in Holanda *et al.* [4]. ($\mathbf{C_1}$ and $\mathbf{C_2}$) African smoke probed over the Atlantic Ocean during CAFE-Africa – here separated into the five flights that probed relevant smoke conditions. ($\mathbf{D_1}$ and $\mathbf{D_2}$) For further comparison, fresh smoke over fires in the Amazonian rain forest vs fires in the Cerrado savanna region probed during the SAMBBA campaign according to Hodgson *et al.* [23]. In the box-whisker plots, the horizontal lines represent the medians, circular markers the means, boxes the 25th and 75th percentiles, and the whiskers the 9th and 91st percentiles. Below, N specifies the number of data points used to compose the box-whisker plots with one data point representing a 3 h- and 10 s-averaged rBC mass size distribution for the ground-based and aircraft data, respectively.
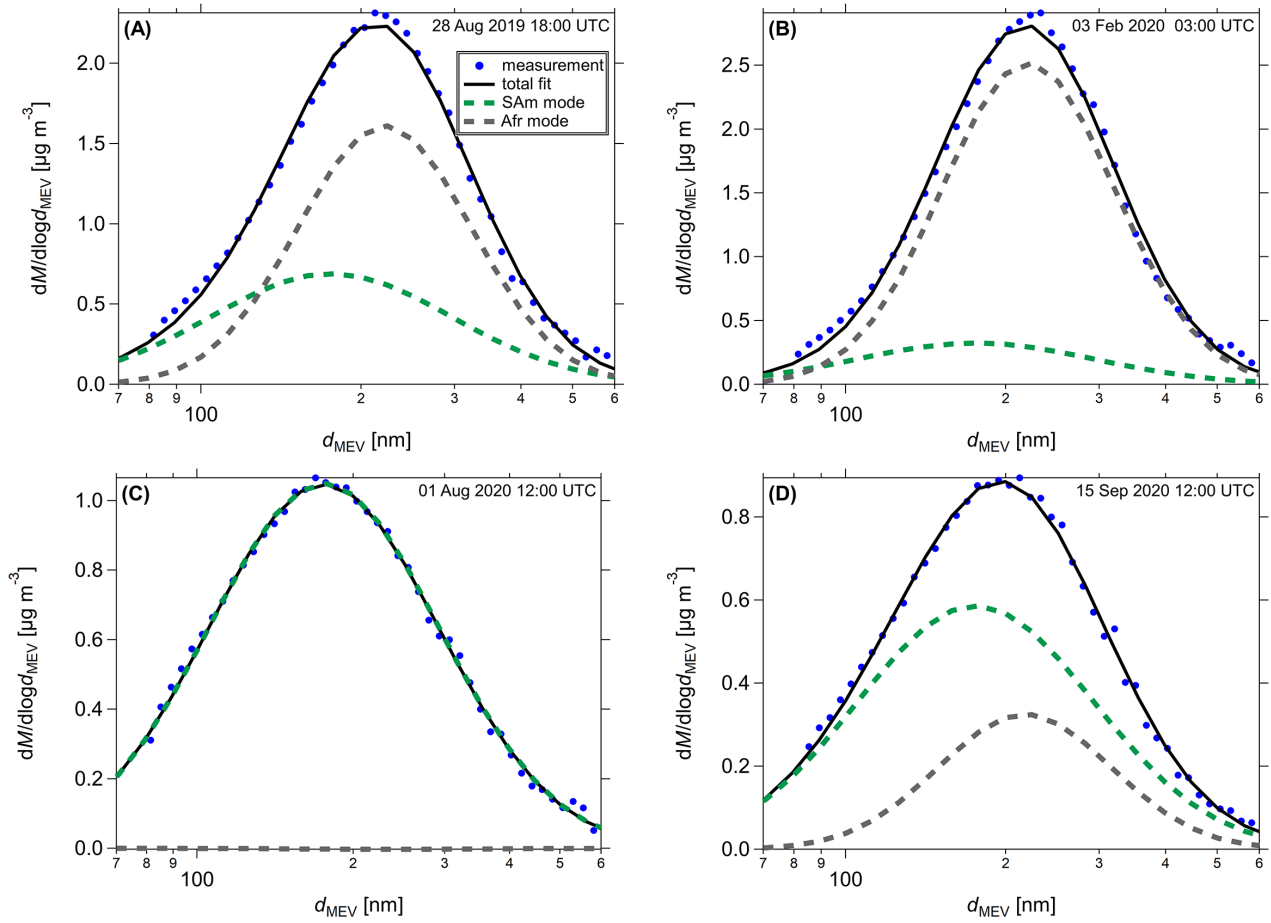
Supplementary Figure 5: Examples of bimodal fits of 3 h-averaged ATTO rBC mass size distributions. The fit comprises an African (Afr) mode and a South American (SAm) mode with constraints for the fit parameters D_{rBC} and σ_{rBC} as outlined in Supplementary Notes 1.3.
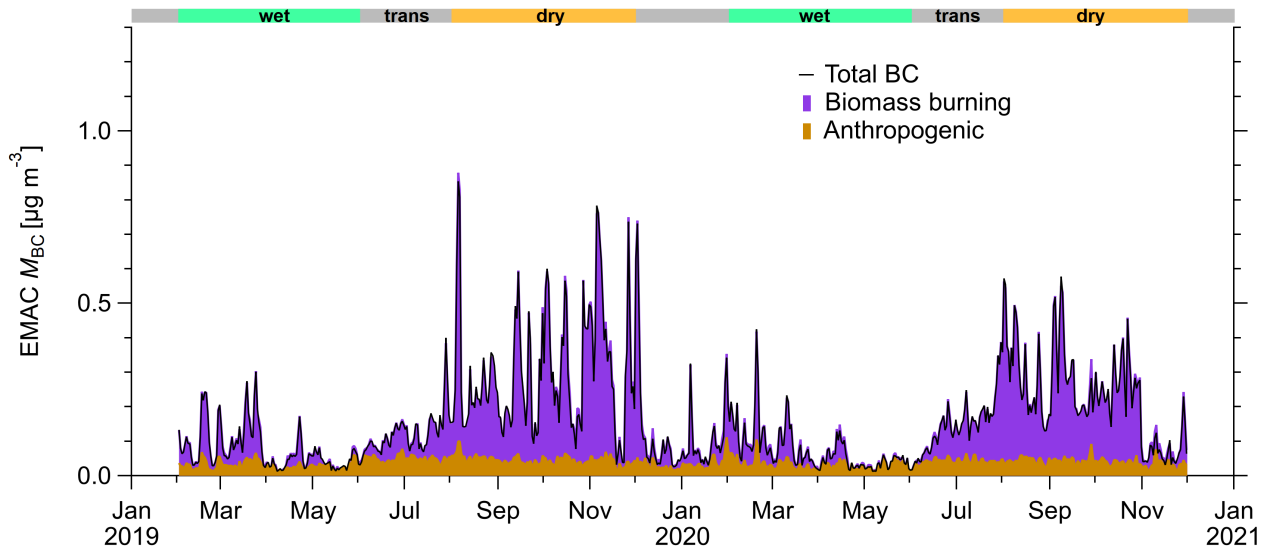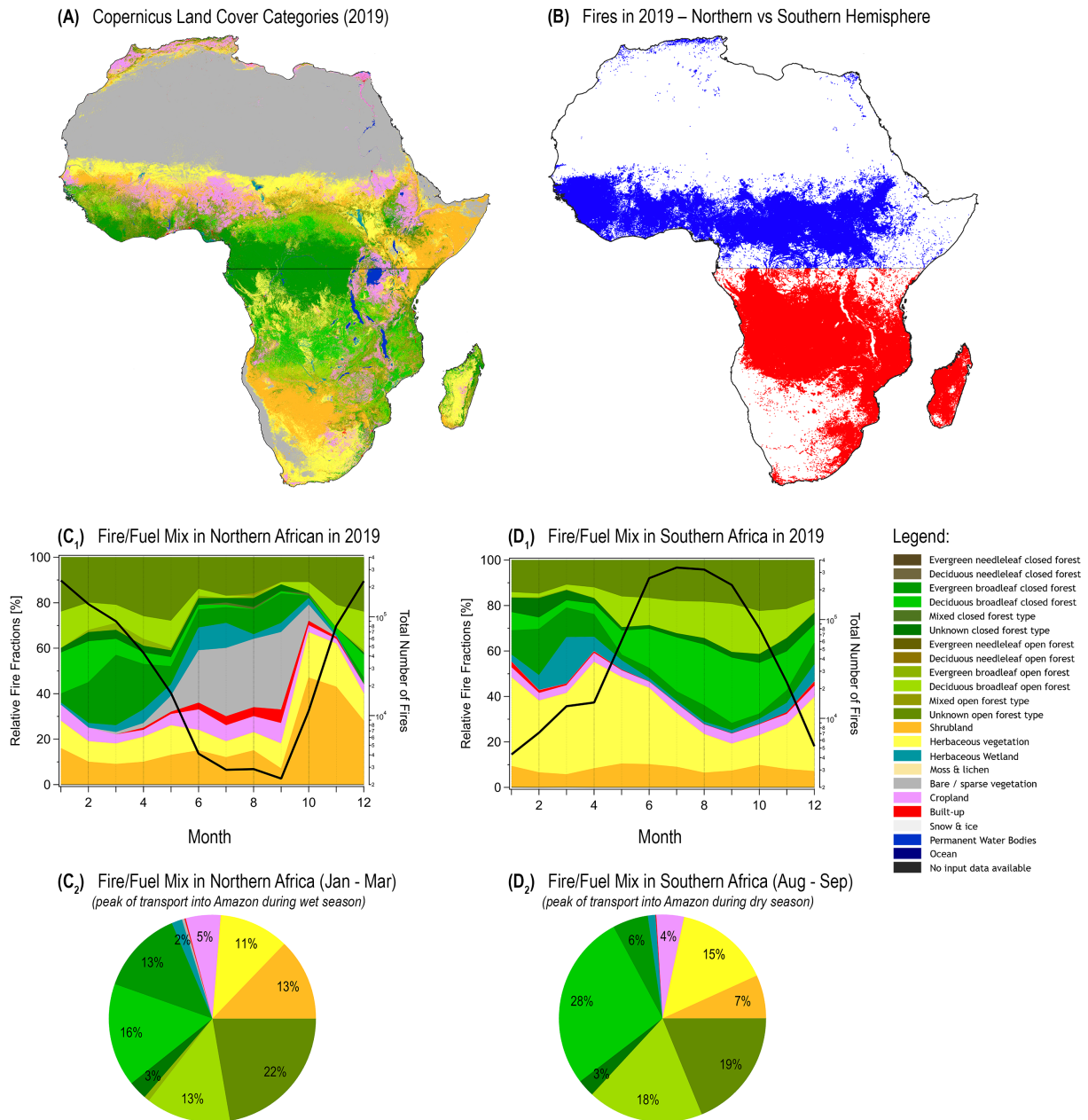
Supplementary Figure 6: EMAC model sensitivity simulation showing the contributions of biomass burning and (other) anthropogenic emissions to the total BC mass concentrations, M_{BC}, at ATTO. The total M_{BC} (black solid line) represents the EMAC standard simulation (STD). Results correspond to the sensitivity test NOANTH as outlined in detail in Sect. 4.10. The anthropogenic sources that were switched on and off here comprise transportation (TRA), industrial combustion and processes (IND), power generation (PGN), residential and commercial combustion (RES), waste incineration (WST), agricultural waste burning (AWB), agricultural soils (AGS), and shipping (SHP).
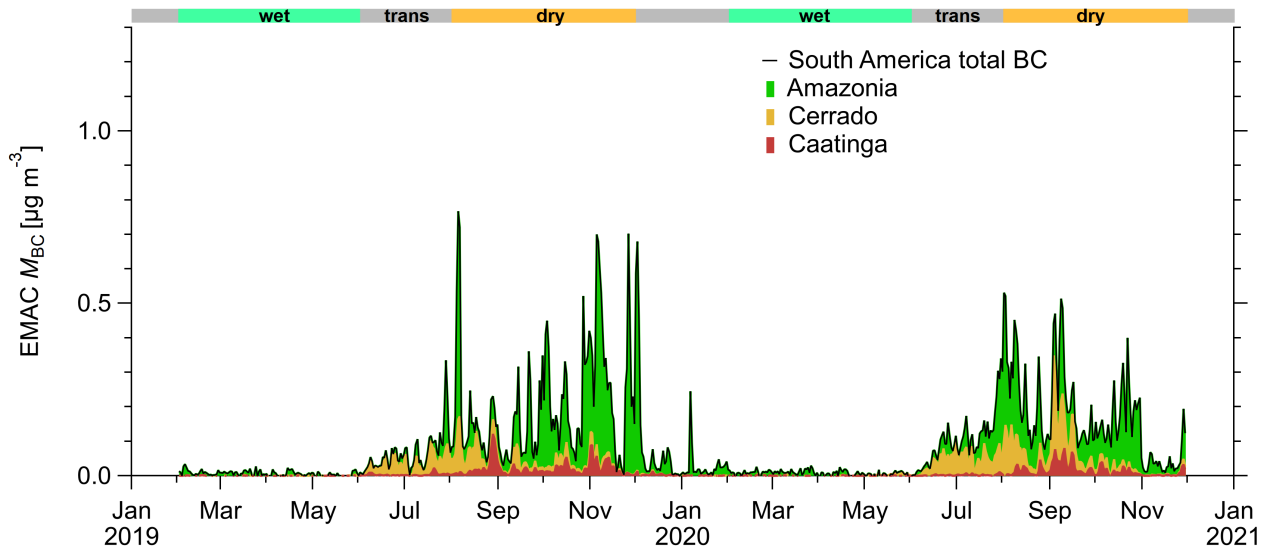
Supplementary Figure 7: EMAC model sensitivity simulation representing the contributions of fires in the Brazilian biomes Amazonia, Cerrado, and Caatinga to the total BC mass concentrations, M_{BC}, at ATTO. The total M_{BC} (black solid line) represents the EMAC standard simulation (STD). Results further include the model runs NOBBcer (zero biomass burning emissions from Cerrado), NOBBcaa (zero biomass burning emission over from Caatinga) as well as NOBB, NOBBafr as outlined in detail in Sect. 4.10. The geographic extent of the ecoregions relative to the ATTO footprint is shown in Supplementary Figure 8.
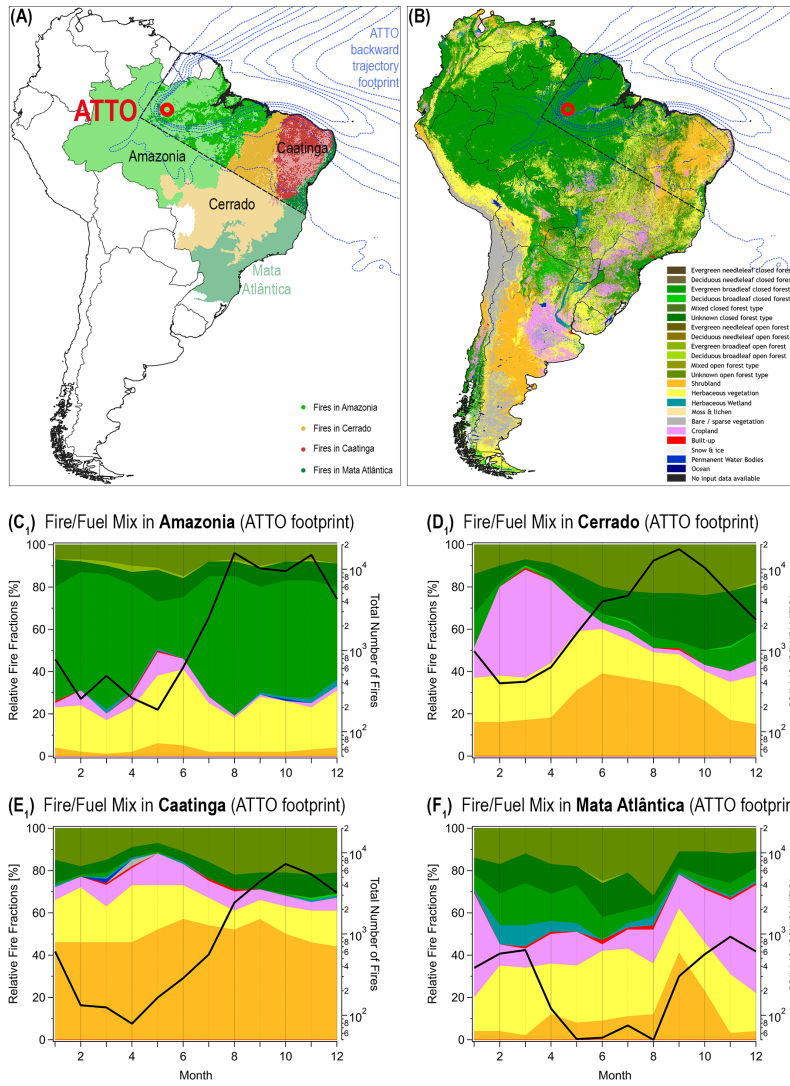
Supplementary Figure 8: Average fire/fuel mixtures in the ATTO footprint region on the South America continent in 2019, separated into the biomes Amazonia, Cerrado, Caatinga, and Mata Atlântica. Fire map (A) and land cover map (B) were combined to calculate the seasonal cycle of fire counts per land cover category (C_1, D_1, E_1, and F_1). Black solid lines in C_1, D_1, E_1, and F_1 show the total number of detected fires. Pie charts in C_2, D_2, E_2, and F_2 emphasize average fire/fuel mixtures in the ATTO footprint-relevant region in the biomes Amazonia, Cerrado, Caatinga, and Mata Atlântica between August and September, which corresponds to the peak of biomass burning in the Amazon. The dashed black polygon line in (A) marks the approximate region of the ATTO footprint (compare the blue isolines representing the backward trajectory contours). For further details, refer to Sect. 4.9.

17

(A) Copernicus Land Cover Categories (2019)

(B) Fires in 2019 – Northern vs Southern Hemisphere

(C$_1$) Fire/Fuel Mix in Northern African in 2019

(D$_1$) Fire/Fuel Mix in Southern Africa in 2019

Legend:
- Evergreen needleleaf closed forest
- Deciduous needleleaf closed forest
- Evergreen broadleaf closed forest
- Deciduous broadleaf closed forest
- Mixed closed forest type
- Unknown closed forest type
- Evergreen needleleaf open forest
- Deciduous needleleaf open forest
- Evergreen broadleaf open forest
- Deciduous broadleaf open forest
- Mixed open forest type
- Unknown open forest type
- Shrubland
- Herbaceous vegetation
- Herbaceous Wetland
- Moss & lichen
- Bare / sparse vegetation
- Cropland
- Built-up
- Snow & ice
- Permanent Water Bodies
- Ocean
- No input data available

(C$_2$) Fire/Fuel Mix in Northern Africa (Jan - Mar)
(peak of transport into Amazon during wet season)

(D$_2$) Fire/Fuel Mix in Southern Africa (Aug - Sep)
(peak of transport into Amazon during dry season)

Supplementary Figure 9: Average fire/fuel mixtures in Africa in 2019, separated into the Northern vs Southern hemispheres. Land cover map (**A**) and fire map (**B**) were combined to calculate the seasonal cycle of fire counts per land cover category (**C$_1$** and **D$_1$**). Black solid lines in **C$_1$** and **D$_1$** show the total number of detected fires. Pie charts in **C$_2$** and **D$_2$** show (i) the average fire/fuel mixture in Northern Africa between January and March, which corresponds to the peak of long-range transport of African smoke into the Amazon during the wet season and (ii) the average fire/fuel mixture in Southern Africa between August and September, which corresponds to the peak of long-range transport of African smoke into the Amazon during the dry season. For further details, refer to Sect. 4.9.

18
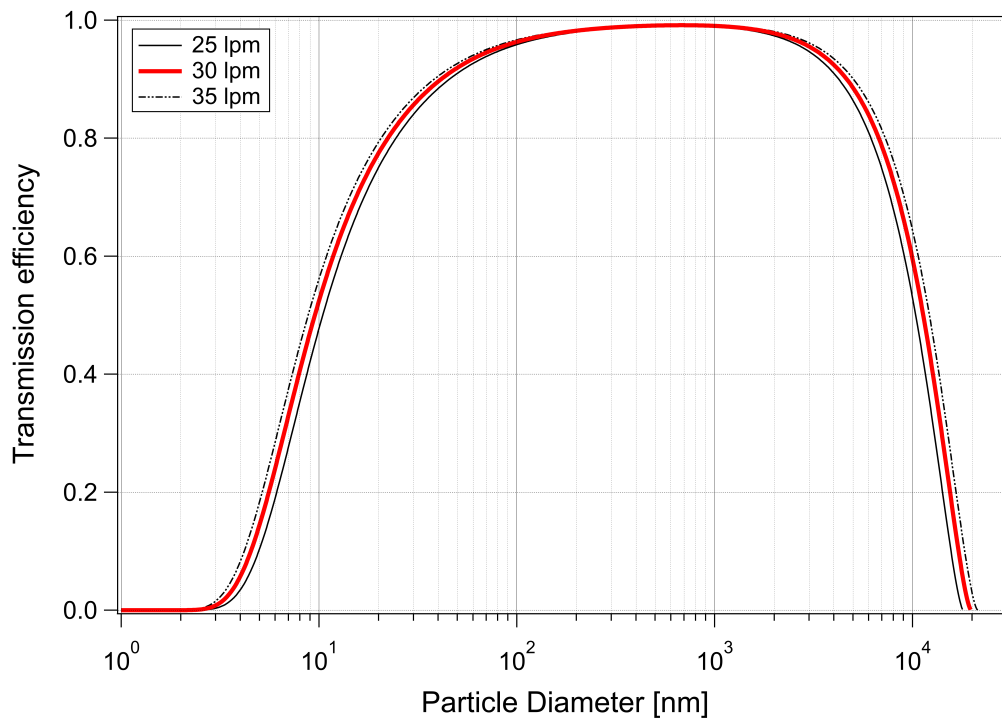
Supplementary Figure 10: Calculated transmission efficiency of the 325 m aerosol inlet at the tall tower at ATTO. The transmission curve was calculated for three different sample air flow rates in the main inlet tube by using the particle loss calculator (PLC, version 2.0) developed by von der Weiden *et al.* [43]. Refer also to Supplementary materials in Moran-Zuloaga *et al.* [2].
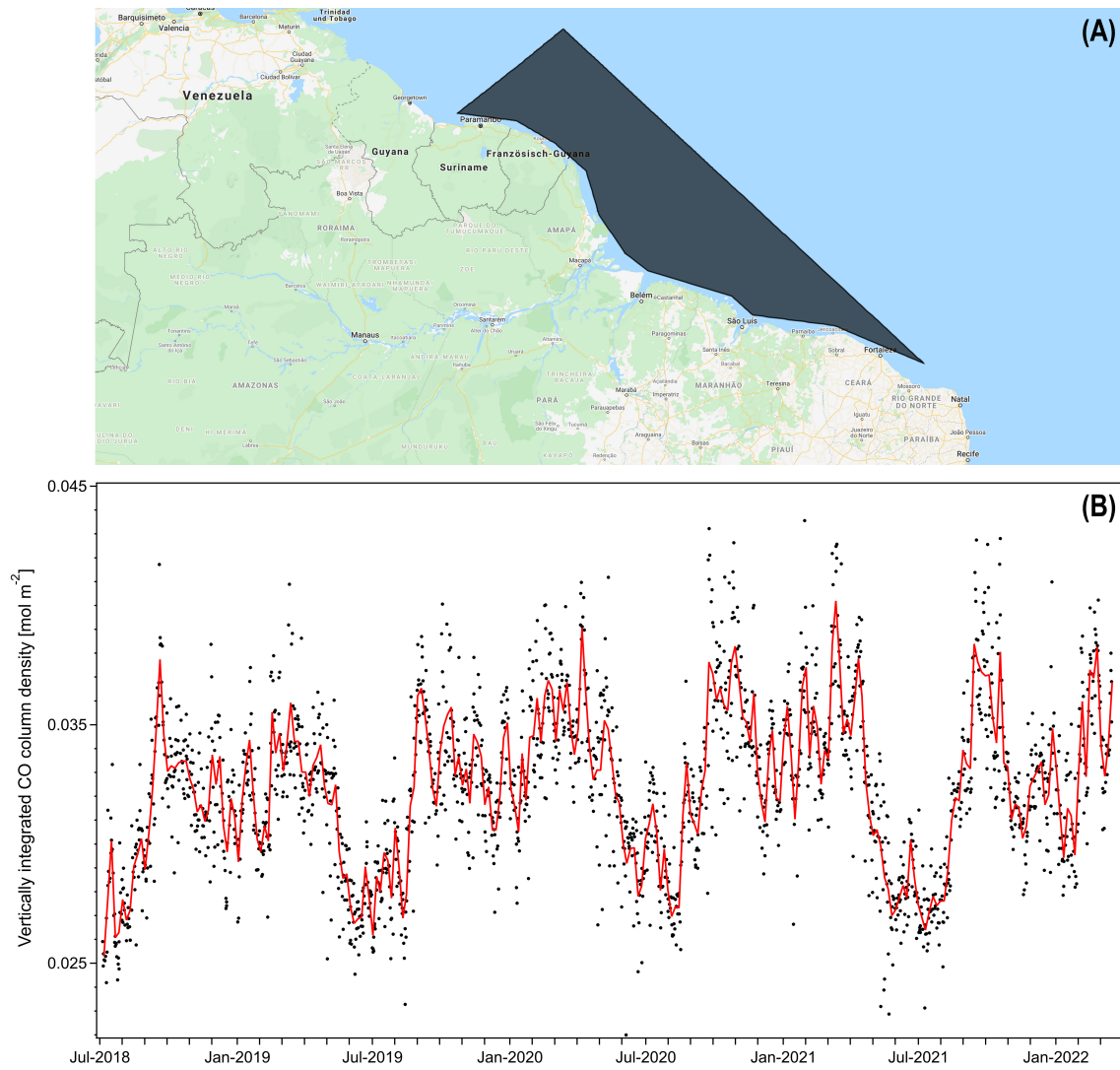
Supplementary Figure 11: Satellite-derived vertically integrated CO column density in the offshore region of interest (ROI$_{offshore}$) in front of South American coast as proxy for African smoke influx into the Amazon. **(A)** Map showing location and shape of the ROI$_{offshore}$. **(B)** Corresponding time series of the vertically integrated CO column density (CO$_{ROI}$) within ROI$_{offshore}$. The figure shows individual data points (black dots) and the 5-day averages (solid line). For details refer to Sect. 4.5.
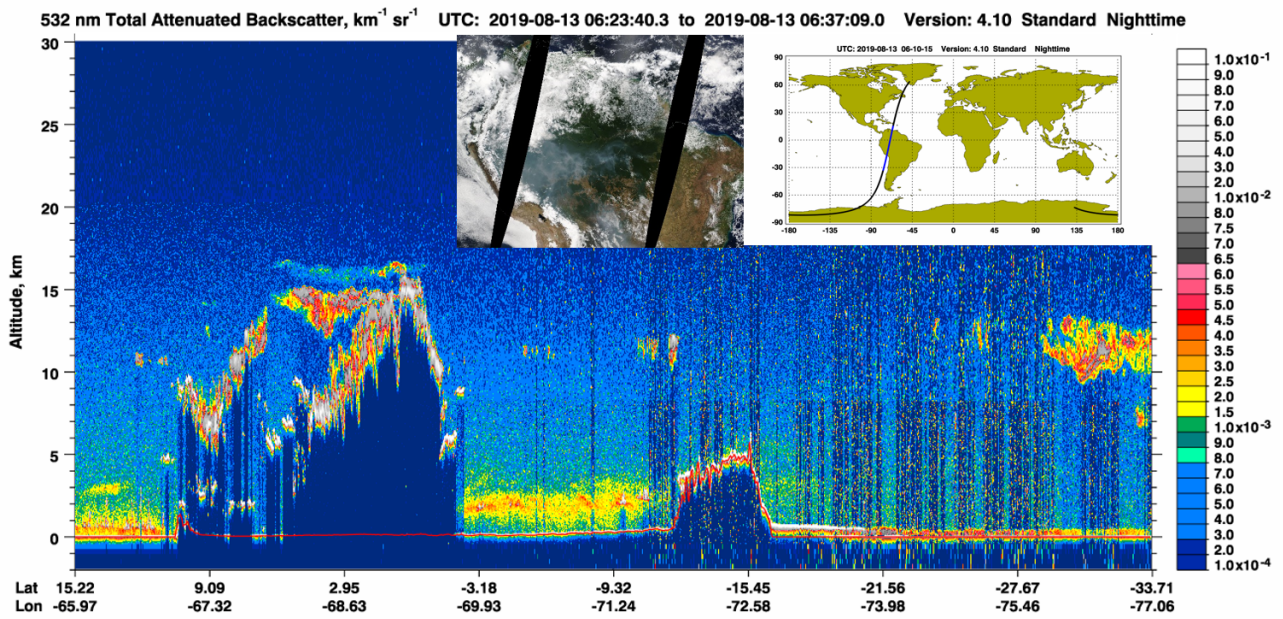
Supplementary Figure 12: Exemplary lidar profiles from CALIPSO (https://www-calipso.larc.nasa.gov/, last access 04 Sep 2021) passage on 13 August 2019 over the smoky western Amazon basin showing enrichment of the smoke in the lower 2 to 3 km of the atmosphere. The CALIPSO orbit for this particular scene is shown in the upper right corner. A true color image of the same day is shown in the upper middle.
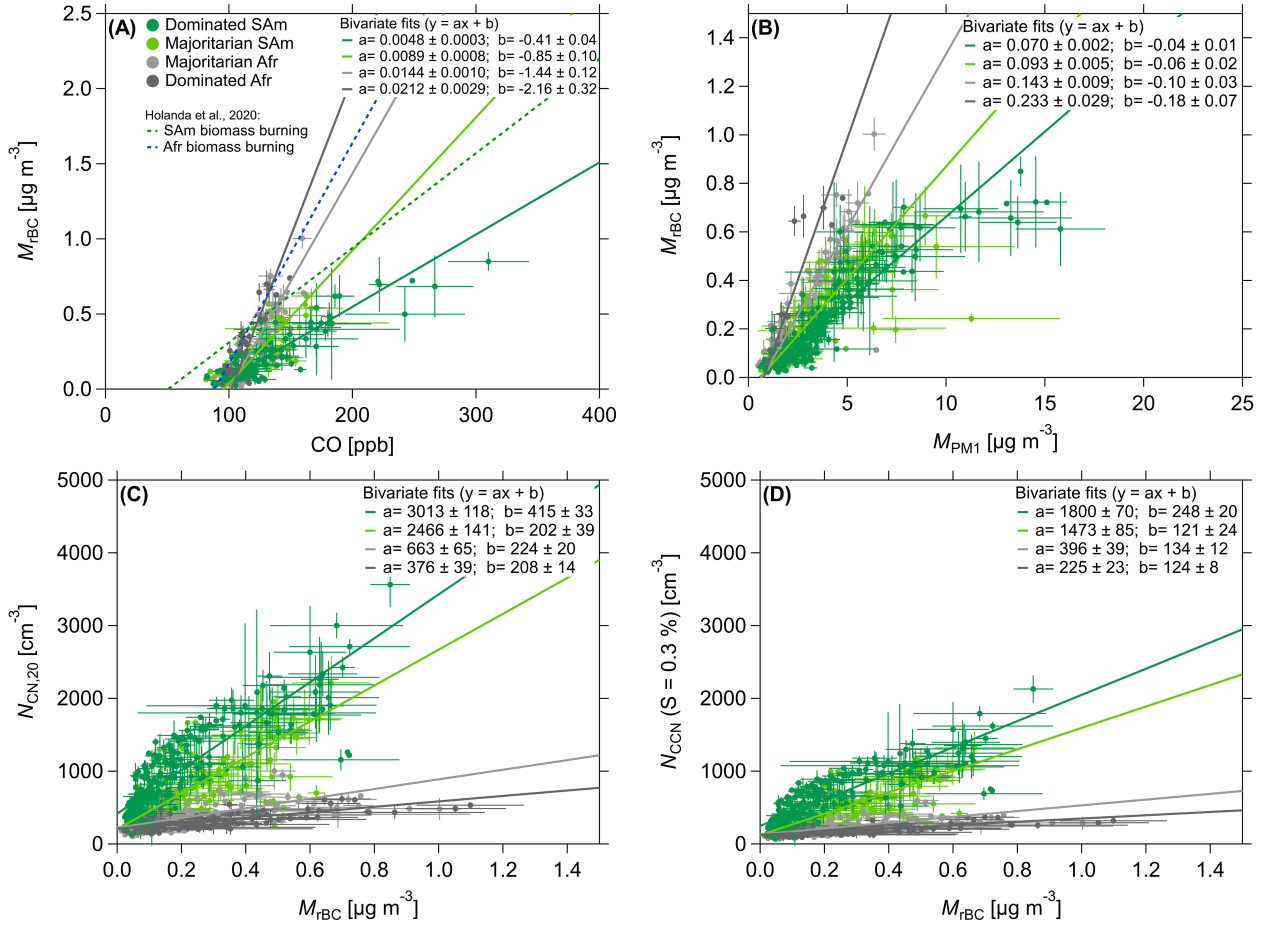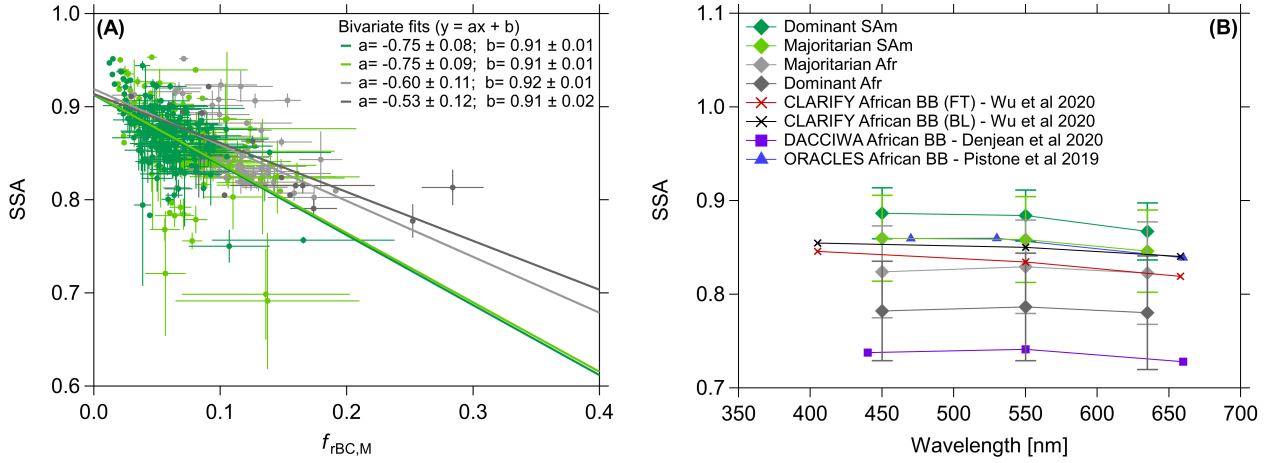
Supplementary Figure 13: Correlations between selected aerosol and trace gas parameters, separated into into the four categories of dominant or majoritarian South American influence vs dominant or majoritarian African influence. Specifically shown are **(A)** black carbon mass concentration (M_{rBC}) vs carbon monoxide (CO); **(B)** M_{rBC} vs total submicrometer aerosol mass (M_{PM1}) derived from SP2 and ACSM; **(C)** total particle number concentration with $D_p > 20$ nm ($N_{CN,20}$) vs black carbon mass concentration (M_{rBC}); **(D)** cloud condensation nuclei number concentration N_{CCN} at a supersaturation of 0.3 % vs M_{rBC}; The solid lines represent linear orthogonal distance regression (ODR) fits applied to the daily averaged data with error bars showing the standard deviations. Further shown in **(A)** as dashed lines are previous results from a related study by Holanda et al. [4].
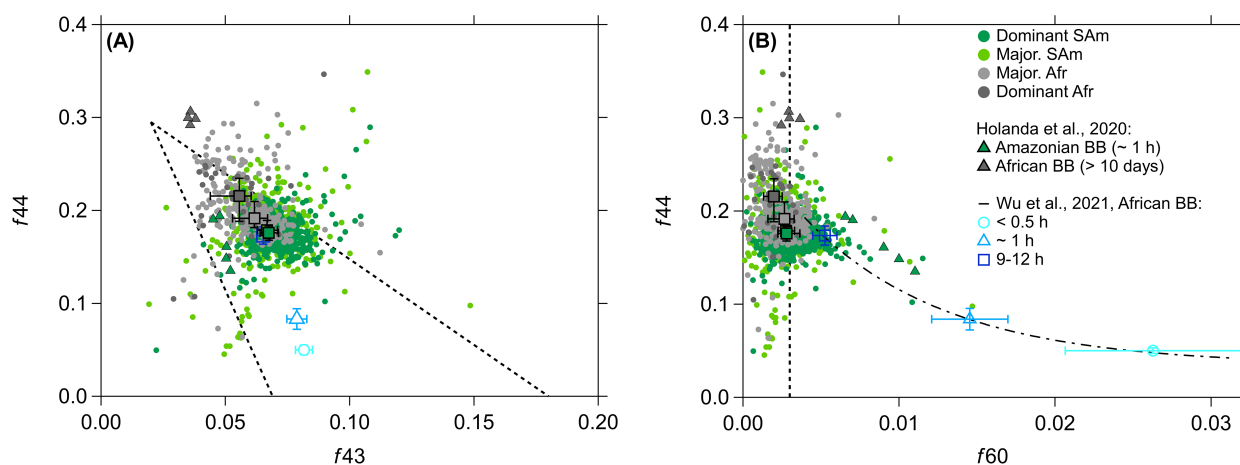
Supplementary Figure 14: ACSM results reflecting the extent of photo-chemical aging of the organic aerosol constituents and confirming that the African smoke at ATTO is strongly aged, whereas the South American smoke is comparatively fresh. **(A)** Scatter plot of the ratios $f43$ (m/z 43 to total organic signal) against $f44$ (m/z 44 to total organic signal) with the m/z 44 signal relating mostly to CO_2^+ ions and the m/z 43 signal to $C_2H_3O^+$ ions. The triangular region (dashed lines) in the $f44$ vs $f43$ space defines the boundaries within which most of the organic aerosol was found in previous studies [34, 44]. Data in the upper left represent more oxidized organics vs the less oxidized organics in the lower right. **(B)** Scatter plot of the ratios $f44$ (m/z 44 to total organic signal) against $f60$ (m/z 60 to total organic signal) with the m/z 60 signal relating to the biomass burning tracer, levoglucosan. The vertical dashed line in **(B)** represents the reference value for negligible influence of comparatively fresh smoke according to Cubison *et al.* [33], either because biomass burning influence is absent or levoglucosan has been completely oxidized. The curved dashed line in **(B)** represents the temporal evolution in $f44$ vs $f60$ space of smoke upon aging right after emission according to Wu *et al.* [20]. Further shown are the markers from our previous study Holanda *et al.* [4] showing aged African and rather fresh Amazonian smoke.
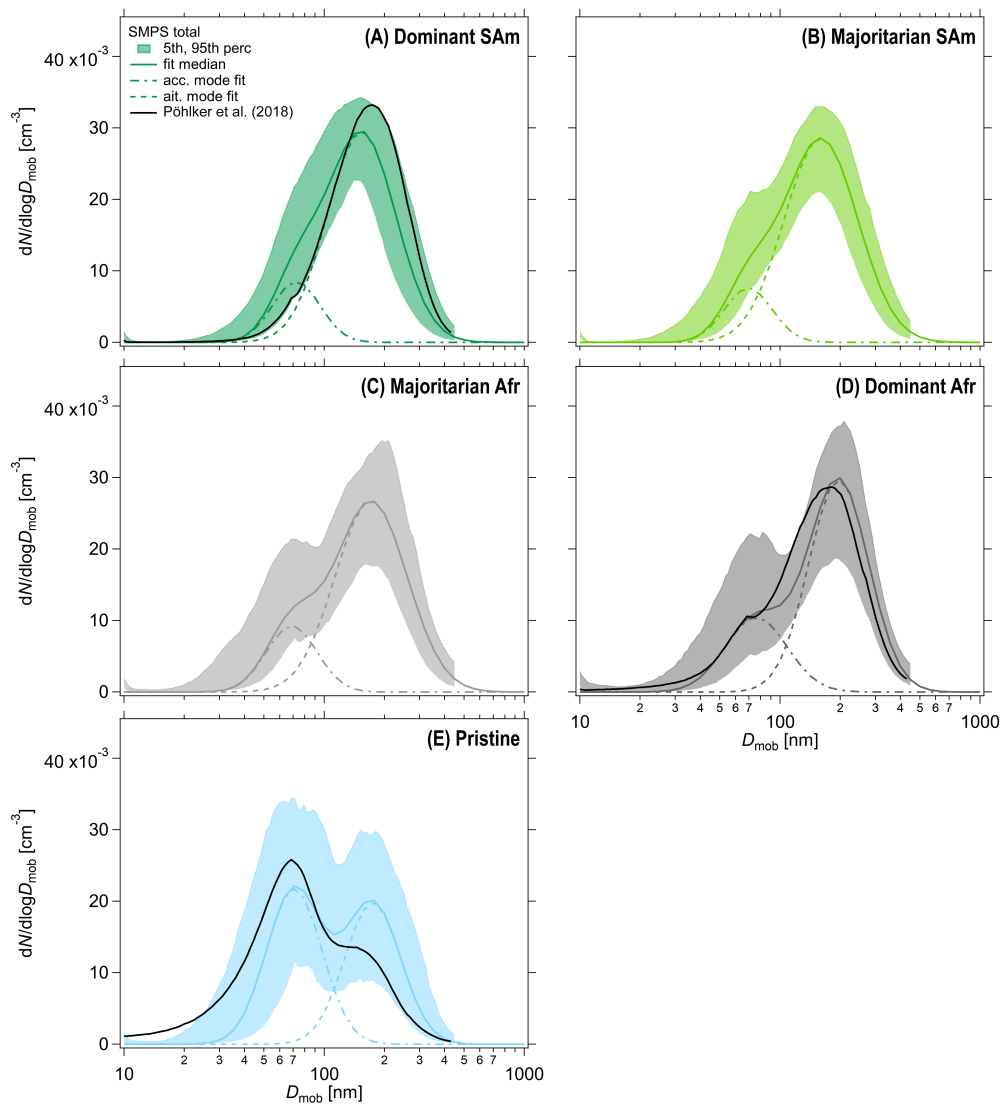
Supplementary Figure 15: Statistical analysis of the particle number size distributions (PNSD, normalized by the area below the curve) under different atmospheric conditions at ATTO: (A) dominant South American; (B) majoritarian South America; (C) majoritarian Africa; (D) dominant Africa and (E) pristine aerosol conditions. Solid lines represent the bimodal fitted log-normal function with shadings corresponding to the 5th to 95th percentile ranges. Panels (A), (D) and (E) also shows the PNSDs for the *biomass burning*, *long-range-transport* and *pristine* case studies reported in Pöhlker *et. al.* [27].
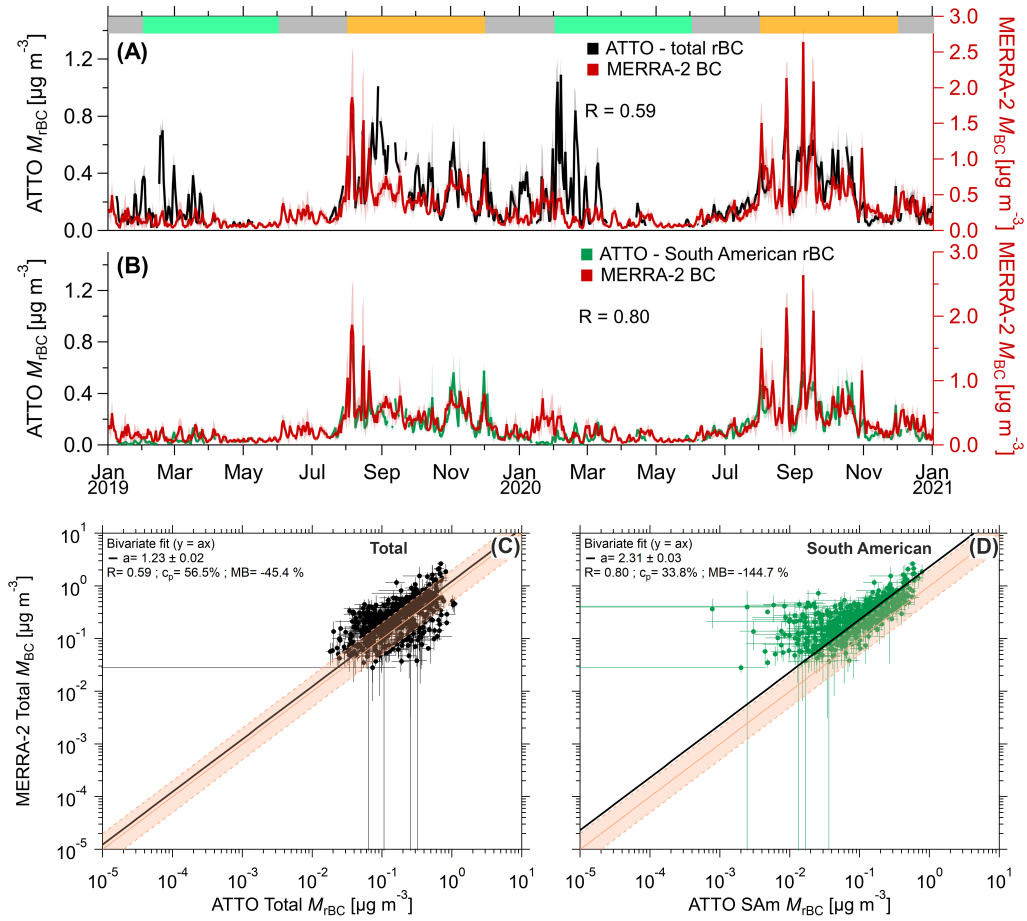
Supplementary Figure 16: **(A)** Correlations between single scattering albedo (SSA) at 637 nm vs rBC mass fraction ($f_{rBC,M}$); and **(B)** wavelength dependence of single scattering albedo (SSA) for the four categories of smoke conditions at ATTO, which are dominant or majoritarian South American influence vs dominant or majoritarian African influence. For comparison, SSA values in African smoke plumes from the previous campaigns CLARIFY [40], ORACLES [45] and DACCIWA [39] are shown. The SSA was calculated by interpolating the measured absorption coefficient from the Aethalometer at 3 wavelengths.
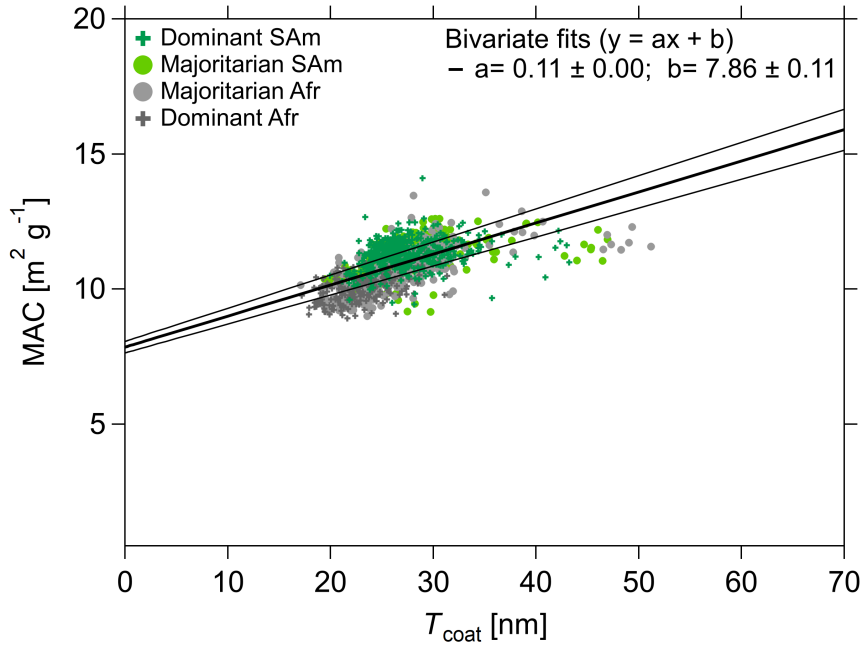
Supplementary Figure 17: Relationship between mass absorption cross section (MAC) at 637 nm and the average coating thickness (T_{coat}) on rBC cores in the diameter range $180 < d_{MEV} < 220$ nm for the four categories of smoke conditions at ATTO, which are dominant or majoritarian South American influence vs dominant or majoritarian African influence. Compare also Supplementary Figure 13F. The MAC of the bare BC ($MAC_{BC,bare}$) of $\sim 8\,m^2\,g^{-1}$ was obtained from the y-axis intercept of the orthogonal linear fit, consistent with the values in previous studies [39, 46].
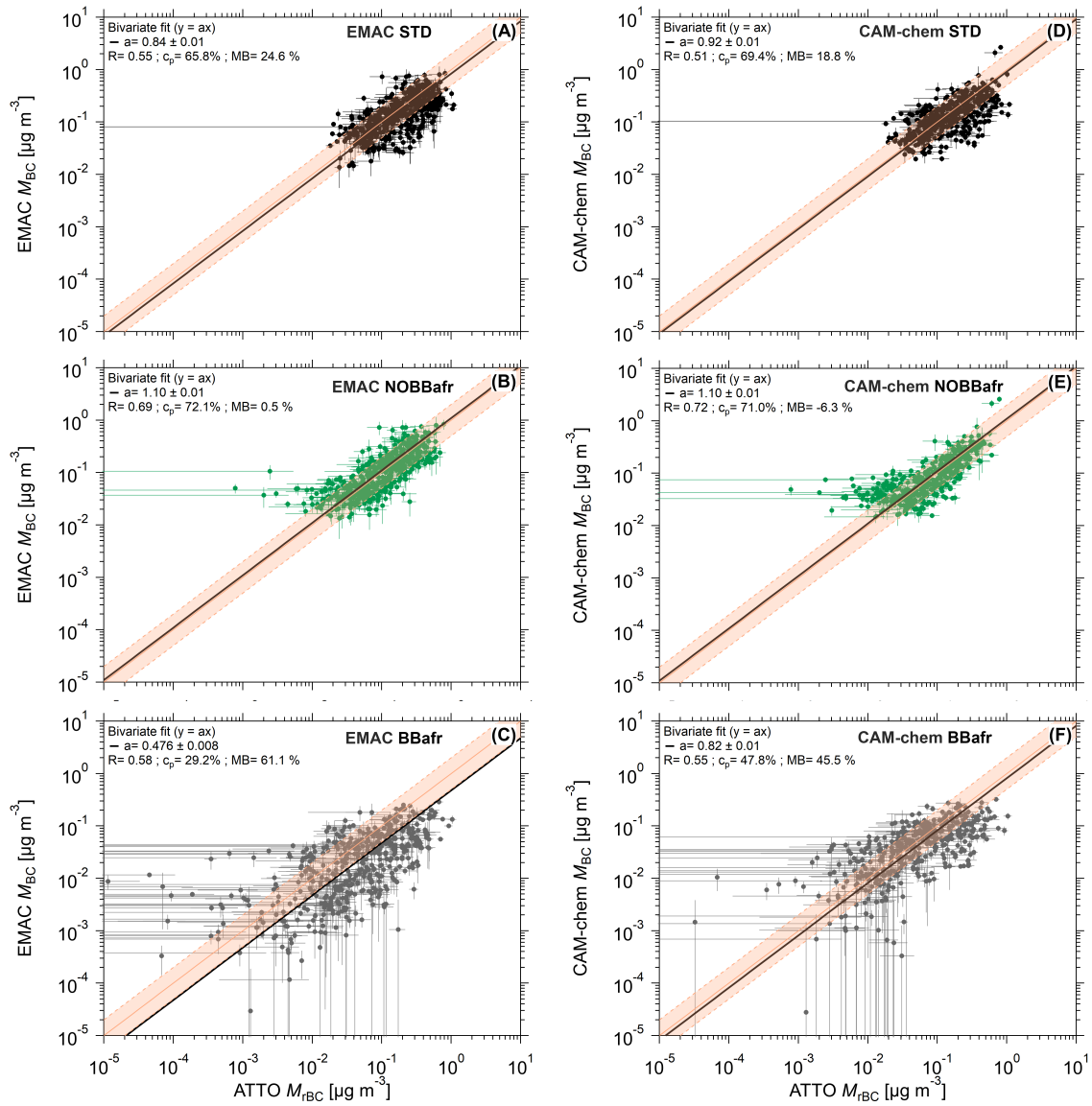
Supplementary Figure 18: Correlations between measured and modelled BC mass concentrations (M_{BC}) at ATTO , in relation to corresponding time series in Fig. 5. The following cases are shown: **A** and **D**: total BC (black markers, STD model runs), **B** and **E**: the South American BC fraction (green markers, NOBBafr model runs), and **C** and **F**: the African BC fraction (gray markers, model run BBafr = STD - NOBBafr). EMAC (**A**–**C**, see Supplementary Notes 4.10) and CAM-chem (**D**–**F**, see Supplementary Notes 4.11) model results are compared here. Shaded area represents the region between the 1:2 and 2:1 lines. Specified in the individual panels are the fit parameters, the correlation coefficient (R), the percentage of data points (c_p) that fall between the 1:2 and 2:1 lines, and the mean bias between model and observation (MB).

Supplementary Figure 19: Comparison between MERRA-2 reanalysis and ATTO observations. **(A − B)** Time series of total (M_{rBC}, black line) as well as South American ($M_{rBC,SAm}$, green) BC mass concentration measured at ATTO (data from Fig. 3) and BC surface mass concentration from MERRA-2 ($M_{BC,MERRA}$, red) averaged over the area that includes ATTO ($-60 <$ Lon $<-58.125°$ E; $-2.5 <$ Lat $<-1.5°$ N). All time series show daily averages with colored shading as standard deviation. The legend specifies the Pearson's R for relationship between experimental and model data. **(C − D)** Correlations between measured and modelled BC mass concentrations (M_{BC}) at ATTO, in relation to corresponding time series in (A − B). The shaded area represents the region between the 1:2 and 2:1 lines. Specified in the individual panels are the fit parameters, the correlation coefficient (R), the percentage of data points (c_p) that fall between the 1:2 and 2:1 lines, and the mean bias between model and observation (MB). Beyond Supplementary Figure 18, here the agreement with the MERRA-2 reanalysis is shown. Note that only the total BC at ATTO was derived from MERRA-2.

4 Supplementary References

References

[1] A. E. Barkley, J. M. Prospero, N. Mahowald, D. S. Hamilton, K. J. Popendorf, A. M. Oehlert, A. Pourmand, A. Gatineau, K. Panechou-Pulcherie, P. Blackwelder, C. J. Gaston, African biomass burning is a substantial source of phosphorus deposition to the Amazon, Tropical Atlantic Ocean, and Southern Ocean, *Proceedings of the National Academy of Sciences* **116**, 16216–16221 (2019).

[2] D. Moran-Zuloaga, F. Ditas, D. Walter, J. Saturno, J. Brito, S. Carbone, X. Chi, I. Hrabě de Angelis, H. Baars, R. H. M. Godoi, B. Heese, B. A. Holanda, J. V. Lavrič, S. T. Martin, J. Ming, M. L. Pöhlker, N. Ruckteschler, H. Su, Y. Wang, Q. Wang, Z. Wang, B. Weber, S. Wolff, P. Artaxo, U. Pöschl, M. O. Andreae, C. Pöhlker, Long-term study on coarse mode aerosols in the Amazon rain forest with the frequent intrusion of Saharan dust plumes, *Atmos. Chem. Phys.* **18**, 10055–10088 (2018).

[3] Q. Wang, J. Saturno, X. Chi, D. Walter, J. V. Lavric, D. Moran-Zuloaga, F. Ditas, C. Pöhlker, J. Brito, S. Carbone, P. Artaxo, M. O. Andreae, Modeling investigation of light-absorbing aerosols in the Amazon Basin during the wet season, *Atmospheric Chemistry and Physics* **16**, 14775–14794 (2016).

[4] B. A. Holanda, M. L. Pöhlker, D. Walter, J. Saturno, M. Sörgel, J. Ditas, F. Ditas, C. Schulz, M. A. Franco, Q. Wang, T. Donth, P. Artaxo, H. M. J. Barbosa, S. Borrmann, R. Braga, J. Brito, Y. Cheng, M. Dollner, J. W. Kaiser, T. Klimach, C. Knote, O. O. Krüger, D. Fütterer, J. V. Lavrič, N. Ma, L. A. T. Machado, J. Ming, F. G. Morais, H. Paulsen, D. Sauer, H. Schlager, J. Schneider, H. Su, B. Weinzierl, A. Walser, M. Wendisch, H. Ziereis, M. Zöger, U. Pöschl, M. O. Andreae, C. Pöhlker, Influx of African biomass burning aerosol during the Amazonian dry season through layered transatlantic transport of black carbon-rich smoke, *Atmos. Chem. Phys.* **20**, 4757–4785 (2020).

[5] J. Saturno, B. A. Holanda, C. Pöhlker, F. Ditas, Q. Wang, D. Moran-Zuloaga, J. Brito, S. Carbone, Y. Cheng, X. Chi, J. Ditas, T. Hoffmann, I. Hrabe de Angelis, T. Könemann, J. V. Lavrič, N. Ma, J. Ming, H. Paulsen, M. L. Pöhlker, L. V. Rizzo, P. Schlag, H. Su, D. Walter, S. Wolff, Y. Zhang, P. Artaxo, U. Pöschl, M. O. Andreae, Black and brown carbon over central Amazonia: long-term aerosol measurements at the ATTO site, *Atmos. Chem. Phys.* **18**, 12817–12843 (2018).

[6] H. Baars, A. Ansmann, D. Althausen, R. Engelmann, B. Heese, D. Mller, P. Artaxo, M. Paixao, T. Pauliquevis, R. Souza, Aerosol profiling with lidar in the Amazon Basin during the wet and dry season, *Journal of Geophysical Research Atmospheres* **117**, 1–16 (2012).

[7] D. Liu, J. D. Allan, D. E. Young, H. Coe, D. Beddows, Z. L. Fleming, M. J. Flynn, M. W. Gallagher, R. M. Harrison, J. Lee, A. S. H. Prevot, J. W. Taylor, J. Yin, P. I. Williams, P. Zotter, Size distribution, mixing state and source apportionment of black carbon aerosol in London during wintertime, *Atmospheric Chemistry and Physics* **14**, 10061–10084 (2014).

[8] C. Pöhlker, D. Walter, H. Paulsen, T. Könemann, E. Rodríguez-Caballero, D. Moran-Zuloaga, J. Brito, S. Carbone, C. Degrendele, V. R. Després, F. Ditas, B. A. Holanda, J. W. Kaiser, G. Lammel, J. V. Lavrič, J. Ming, D. Pickersgill, M. L. Pöhlker, M. Praß, N. Löbs, J. Saturno, M. Sörgel, Q. Wang, B. Weber, S. Wolff, P. Artaxo, U. Pöschl, M. O. Andreae, Land cover and its transformation in the backward trajectory footprint region of the Amazon Tall Tower Observatory, *Atmos. Chem. Phys.* **19**, 8425–8470 (2019).

[9] C. Pöhlker, K. T. Wiedemann, B. Sinha, M. Shiraiwa, S. S. Gunthe, M. Smith, H. Su, P. Artaxo, Q. Chen, Y. F. Cheng, W. Elbert, M. K. Gilles, A. L. D. Kilcoyne, R. C. Moffet, M. Weigand, S. T. Martin, U. Pöschl, M. O. Andreae, Biogenic Potassium Salt Particles as Seeds for Secondary Organic Aerosol in the Amazon, *Science* **337**, 1075–1078 (2012).

[10] N. Moteki, Y. Kondo, N. Oshima, N. Takegawa, M. Koike, K. Kita, H. Matsui, M. Kajino, Size dependence of wet removal of black carbon aerosols during transport from the boundary layer to the free troposphere, *Geophysical Research Letters* **39**, 2–5 (2012).

[11] J. P. Schwarz, R. S. Gao, J. R. Spackman, L. A. Watts, D. S. Thomson, D. W. Fahey, T. B. Ryerson, J. Peischl, J. S. Holloway, M. Trainer, G. J. Frost, T. Baynard, D. A. Lack, J. A. de Gouw, C. Warneke, L. A. Del Negro, Measurement of the mixing state, mass, and optical size of individual black carbon particles in urban and biomass burning emissions, *Geophysical Research Letters* **35**, 1–5 (2008).

[12] M. Laborde, M. Crippa, T. Tritscher, Z. Jurányi, P. F. Decarlo, B. Temime-Roussel, N. Marchand, S. Eckhardt, A. Stohl, U. Baltensperger, A. S. Prévôt, E. Weingartner, M. Gysel, Black carbon physical properties and mixing state in the European megacity Paris, *Atmospheric Chemistry and Physics* **13**, 5831–5856 (2013).

[13] A. A. May, G. R. McMeeking, T. Lee, J. W. Taylor, J. S. Craven, I. Burling, A. P. Sullivan, S. Akagi, J. L. Collett, M. Flynn, H. Coe, S. P. Urbanski, J. H. Seinfeld, R. J. Yokelson, S. M. Kreidenweis, Aerosol emissions from prescribed fires in the United States: A synthesis of laboratory and aircraft measurements, *Journal of Geophysical Research-Atmospheres* **119**, 11826–11849 (2014).

[14] A. L. Holder, G. S. W. Hagler, J. Aurell, M. D. Hays, B. K. Gullett, Particulate matter and black carbon optical properties and emission factors from prescribed fires in the southeastern United States, *Journal of Geophysical Research: Atmospheres* **121**, 3465–3483 (2016).

[15] G. Motos, J. Schmale, J. C. Corbin, R. L. Modini, N. Karlen, M. Bertò, U. Baltensperger, M. Gysel-Beer, Cloud droplet activation properties and scavenged fraction of black carbon in liquid-phase clouds at the high-alpine research station Jungfraujoch (3580ma.s.l.), *Atmospheric Chemistry and Physics* **19**, 3833–3855 (2019).

[16] M. O. Andreae, E. V. Browell, M. Garstang, G. L. Gregory, R. C. Harriss, G. F. Hill, D. J. Jacob, M. C. Pereira, G. W. Sachse, A. W. Setzer, P. L. S. Dias, R. W. Talbot, A. L. Torres, S. C. Wofsy, Biomass-burning emissions and associated haze layers over Amazonia, *Journal of Geophysical Research* **93**, 1509 (1988).

[17] A. Ansmann, H. Baars, M. Tesche, D. Müller, D. Althausen, R. Engelmann, T. Pauliquevis, P. Artaxo, Dust and smoke transport from Africa to South America: Lidar profiling over Cape Verde and the Amazon rainforest, *Geophysical Research Letters* **36**, L11802 (2009).

[18] L. Fierce, N. Riemer, T. C. Bond, Explaining variance in black carbon's aging timescale, *Atmospheric Chemistry and Physics* **15**, 3173–3191 (2015).

[19] J. H. Seinfeld, S. N. Pandis, *Atmospheric Chemistry and Physics: From Air Pollution to Climate Change* (John Wiley & Sons, Inc., 2006).

[20] H. Wu, J. W. Taylor, J. M. Langridge, C. Yu, J. D. Allan, K. Szpek, M. I. Cotterell, P. I. Williams, M. Flynn, P. Barker, C. Fox, G. Allen, J. Lee, H. Coe, Rapid transformation of ambient absorbing aerosols from West African biomass burning, *Atmospheric Chemistry and Physics* **21**, 9417–9440 (2021).

[21] J. W. Taylor, H. Wu, K. Szpek, K. Bower, I. Crawford, M. J. Flynn, P. I. Williams, J. Dorsey, J. M. Langridge, M. I. Cotterell, C. Fox, N. W. Davies, J. M. Haywood, H. Coe, Absorption closure in highly aged biomass burning smoke, *Atmospheric Chemistry and Physics* **20**, 11201–11221 (2020).

[22] J. M. Lobert, J. Wamatz, *Emissions from the combustion process in vegetation* (John Wiley, New York, 1993), pp. 15–37.

[23] A. K. Hodgson, W. T. Morgan, S. O. Shea, S. Bauguitte, J. D. Allan, E. Darbyshire, M. J. Flynn, D. Liu, J. Lee, B. Johnson, J. M. Haywood, K. M. Longo, P. E. Artaxo, H. Coe, Near-field emission profiling of tropical forest and Cerrado fires in Brazil during SAMBBA 2012 pp. 5619–5638 (2018).

[24] J. Heintzenberg, Properties of the Log-Normal Particle Size Distribution, *Aerosol Science and Technology* **21**, 46–48 (1994).

[25] S. T. Martin, M. O. Andreae, P. Artaxo, D. Baumgardner, Q. Chen, A. H. Goldstein, A. Guenther, C. L. Heald, O. L. Mayol-Bracero, P. H. McMurry, T. Pauliquevis, U. Poschl, K. A. Prather, G. C. Roberts, S. R. Saleska, M. A. S. Dias, D. V. Spracklen, E. Swietlicki, I. Trebs, Sources and properties of Amazonian aerosol particles, *Reviews of Geophysics* **48**, RG2002 (2010).

[26] S. Martin, P. Artaxo, L. Machado, A. Manzi, R. Souza, C. Schumacher, J. Wang, T. Biscaro, J. Brito, A. Calheiros, K. Jardine, A. Medeiros, B. Portela, S. d. Sá, K. Adachi, A. Aiken, R. Albrecht, L. Alexander, M. Andreae, H. Barbosa, P. Buseck, D. Chand, J. Comstock, D. Day, M. Dubey, J. Fan, J. Fast, G. Fisch, E. Fortner, S. Giangrande, M. Gilles, A. Goldstein, A. Guenther, J. Hubbe, M. Jensen, J. Jimenez, F. Keutsch, S. Kim, C. Kuang, A. Laskin, K. McKinney, F. Mei, M. Miller, R. Nascimento, T. Pauliquevis, M. Pekour, J. Peres, T. Petäjä, C. Pöhlker, U. Pöschl, L. Rizzo, B. Schmid, J. Shilling, M. S. Dias, J. Smith, J. Tomlinson, J. Tóta, M. Wendisch, The Green Ocean Amazon Experiment (GoAmazon2014/5) Observes Pollution Affecting Gases, Aerosols, Clouds, and Rainfall over the Rain Forest, *Bulletin of the American Meteorological Society* **0**, null (2016).

[27] M. L. Pöhlker, F. Ditas, J. Saturno, T. Klimach, I. Hrabĕ de Angelis, A. C. Araùjo, J. Brito, S. Carbone, Y. Cheng, X. Chi, R. Ditz, S. S. Gunthe, B. A. Holanda, K. Kandler, J. Kesselmeier, T. Könemann, O. O. Krüger, J. V. Lavrič, S. T. Martin, E. Mikhailov, D. Moran-Zuloaga, L. V. Rizzo, D. Rose, H. Su, R. Thalman, D. Walter, J. Wang, S. Wolff, H. M. J. Barbosa, P. Artaxo, M. O. Andreae, U. Pöschl, C. Pöhlker, Long-term observations of cloud condensation nuclei over the Amazon rain forest – Part 2: Variability and characteristics of biomass burning, long-range transport, and pristine rain forest aerosols, *Atmos. Chem. Phys.* **18**, 10289–10331 (2018).

[28] M. O. Andreae, Emission of trace gases and aerosols from biomass burning – an updated assessment, *Atmos. Chem. Phys.* **19**, 8523–8546 (2019).

[29] V. Selimovic, R. J. Yokelson, C. Warneke, J. M. Roberts, J. de Gouw, J. Reardon, D. W. T. Griffith, Aerosol optical properties and trace gas emissions by PAX and OP-FTIR for laboratory-simulated western US wildfires during FIREX, *Atmospheric Chemistry and Physics* **18**, 2929–2948 (2018).

[30] A. A. May, G. R. McMeeking, T. Lee, J. W. Taylor, J. S. Craven, I. Burling, A. P. Sullivan, S. Akagi, J. L. Collett, M. Flynn, H. Coe, S. P. Urbanski, J. H. Seinfeld, R. J. Yokelson, S. M. Kreidenweis, Aerosol emissions from prescribed fires in the United States: A synthesis of laboratory and aircraft measurements, *Journal of Geophysical Research: Atmospheres* **119**, 11,826–11,849 (2014).

[31] S. Korontzi, D. E. Ward, R. A. Susott, R. J. Yokelson, C. O. Justice, P. V. Hobbs, E. A. H. Smithwick, W. M. Hao, Seasonal variation and ecosystem dependence of emission factors for selected trace gases and PM2.5 for southern African savanna fires, *Journal of Geophysical Research: Atmospheres* **108** (2003).

[32] L.-W. A. Chen, P. Verburg, A. Shackelford, D. Zhu, R. Susfalk, J. C. Chow, J. G. Watson, Moisture effects on carbon and nitrogen emission from burning of wildland biomass, *Atmospheric Chemistry and Physics* **10**, 6617–6625 (2010).

[33] M. J. Cubison, A. M. Ortega, P. L. Hayes, D. K. Farmer, D. Day, M. J. Lechner, W. H. Brune, E. Apel, G. S. Diskin, J. A. Fisher, H. E. Fuelberg, A. Hecobian, D. J. Knapp, T. Mikoviny, D. Riemer, G. W. Sachse, W. Sessions, R. J. Weber, A. J. Weinheimer, A. Wisthaler, J. L. Jimenez, Effects of aging on organic aerosol from open biomass burning smoke in aircraft and laboratory studies, *Atmospheric Chemistry and Physics* **11**, 12049–12064 (2011).

[34] C. Schulz, J. Schneider, B. Amorim Holanda, O. Appel, A. Costa, S. S. de Sá, V. Dreiling, D. Fütterer, T. Jurkat-Witschas, T. Klimach, M. Krämer, S. T. Martin, S. Mertes, M. L. Pöhlker, D. Sauer, C. Voigt, B. Weinzierl, H. Ziereis, M. Zöger, M. O. Andreae, P. Artaxo, L. A. T. Machado, U. Pöschl, M. Wendisch, S. Borrmann, Aircraft-based observations of isoprene epoxydiol-derived secondary organic aerosol (IEPOX-SOA) in the tropical upper troposphere over the Amazon region, *Atmospheric Chemistry and Physics Discussions* pp. 1–32 (2018).

[35] S. S. de Sá, B. B. Palm, P. Campuzano-Jost, D. A. Day, W. Hu, G. Isaacman-VanWertz, L. D. Yee, J. Brito, S. Carbone, I. O. Ribeiro, G. G. Cirino, Y. Liu, R. Thalman, A. Sedlacek, A. Funk, C. Schumacher, J. E. Shilling, J. Schneider, P. Artaxo, A. H. Goldstein, R. A. F. Souza, J. Wang, K. A. McKinney, H. Barbosa, M. L. Alexander, J. L. Jimenez, S. T. Martin, Urban influence on the concentration and composition of submicron particulate matter in central Amazonia, *Atmospheric Chemistry and Physics* **18**, 12185–12206 (2018).

[36] S. S. de Sá, L. V. Rizzo, B. B. Palm, P. Campuzano-Jost, D. A. Day, L. D. Yee, R. Wernis, G. Isaacman-VanWertz, J. Brito, S. Carbone, Y. J. Liu, A. Sedlacek, S. Springston, A. H. Goldstein, H. M. J. Barbosa, M. L. Alexander, P. Artaxo, J. L. Jimenez, S. T. Martin, Contributions of biomass-burning, urban, and biogenic emissions to the concentrations and light-absorbing properties of particulate matter in central Amazonia during the dry season, *Atmospheric Chemistry and Physics* **19**, 7973–8001 (2019).

[37] J. Brito, L. V. Rizzo, W. T. Morgan, H. Coe, B. Johnson, J. Haywood, K. Longo, S. Freitas, M. O. Andreae, P. Artaxo, Ground-based aerosol characterization during the South American Biomass Burning Analysis (SAMBBA) field experiment, *Atmospheric Chemistry and Physics* **14**, 12069–12083 (2014).

[38] P. Zuidema, A. J. Sedlacek, C. Flynn, S. Springston, R. Delgadillo, J. Zhang, A. C. Aiken, A. Koontz, P. Muradyan, The Ascension Island Boundary Layer in the Remote Southeast Atlantic is Often Smoky, *Geophysical Research Letters* **45**, 4456–4465 (2018).

[39] C. Denjean, T. Bourrianne, F. Burnet, M. Mallet, N. Maury, A. Colomb, P. Dominutti, J. Brito, R. Dupuy, K. Sellegri, A. Schwarzenboeck, C. Flamant, P. Knippertz, Overview of aerosol optical properties over southern West Africa from DACCIWA aircraft measurements, *Atmospheric Chemistry and Physics* **20**, 4735–4756 (2020).

[40] H. Wu, J. W. Taylor, K. Szpek, J. M. Langridge, P. I. Williams, M. Flynn, J. D. Allan, S. J. Abel, J. Pitt, M. I. Cotterell, C. Fox, N. W. Davies, J. Haywood, H. Coe, Vertical variability of the properties of highly aged biomass burning aerosol transported over the southeast Atlantic during CLARIFY-2017, *Atmospheric Chemistry and Physics* **20**, 12697–12719 (2020).

[41] C. H. L. Silva Junior, A. C. M. Pessoa, N. S. Carvalho, J. B. C. Reis, L. O. Anderson, L. E. O. C. Aragao, The Brazilian Amazon deforestation rate in 2020 is the greatest of the decade, *Nature Ecology & Evolution* **5**, 144–145 (2021).

[42] M. Wendisch, U. Poschl, M. O. Andreae, L. A. MacHado, R. Albrecht, H. Schlager, D. Rosenfeld, S. T. Martin, A. Abdelmonem, A. Afchine, A. C. Araujo, P. Artaxo, H. Aufmhoff, H. M. Barbosa, S. Borrmann, R. Braga, B. Buchholz, M. A. Cecchini, A. Costa, J. Curtius, M. Dollner, M. Dorf, V. Dreiling, V. Ebert, A. Ehrlich, F. Ewald, G. Fisch, A. Fix, F. Frank, D. Futterer, C. Heckl, F. Heidelberg, T. Huneke, E. Jakel, E. Jarvinen, T. Jurkat, S. Kanter, U. Kastner, M. Kenntner, J. Kesselmeier, T. Klimach, M. Knecht, R. Kohl, T. Kolling, M. Kramer, M. Kruger, T. C. Krisna, J. V. Lavric, K. Longo, C. Mahnke, A. O. Manzi, B. Mayer, S. Mertes, A. Minikin, S. Molleker, S. Munch, B. Nillius, K. Pfeilsticker, C. Pohlker, A. Roiger, D. Rose, D. Rosenow, D. Sauer, M. Schnaiter, J. Schneider, C. Schulz, R. A. De Souza, A. Spanu, P. Stock, D. Vila, C. Voigt, A. Walser, D. Walter, R. Weigel, B. Weinzierl, F. Werner, M. A. Yamasoe, H. Ziereis, T. Zinner, M. Zoger, Acridicon-chuva campaign: Studying tropical deep convective clouds and precipitation over amazonia using the New German research aircraft HALO, *Bulletin of the American Meteorological Society* **97**, 1885–1908 (2016).

[43] S. L. von der Weiden, F. Drewnick, S. Borrmann, Particle Loss Calculator – a new software tool for the assessment of the performance of aerosol inlet systems, *Atmos. Meas. Tech.* **2**, 479–494 (2009).

[44] N. L. Ng, M. R. Canagaratna, Q. Zhang, J. L. Jimenez, J. Tian, I. M. Ulbrich, J. H. Kroll, K. S. Docherty, P. S. Chhabra, R. Bahreini, S. M. Murphy, J. H. Seinfeld, L. Hildebrandt, N. M. Donahue, P. F. Decarlo, V. A. Lanz, A. S. Prévôt, E. Dinar, Y. Rudich, D. R. Worsnop, Organic aerosol components observed in Northern Hemispheric datasets from Aerosol Mass Spectrometry, *Atmospheric Chemistry and Physics* **10**, 4625–4641 (2010).

[45] K. Pistone, J. Redemann, S. Doherty, P. Zuidema, S. Burton, B. Cairns, S. Cochrane, R. Ferrare, C. Flynn, S. Freitag, S. G. Howell, M. Kacenelenbogen, S. LeBlanc, X. Liu, K. S. Schmidt, A. J. Sedlacek III, M. Segal-Rozenhaimer, Y. Shinozuka, S. Stamnes, B. van Diedenhoven, G. Van Harten, F. Xu, Intercomparison of biomass burning aerosol optical properties from in situ and remote-sensing instruments in ORACLES-2016, *Atmospheric Chemistry and Physics* **19**, 9181–9208 (2019).

[46] J. Yuan, R. L. Modini, M. Zanatta, A. B. Herber, T. Müller, B. Wehner, L. Poulain, T. Tuch, U. Baltensperger, M. Gysel-Beer, Variability in the mass absorption cross section of black carbon (BC) aerosols is driven by BC internal mixing state at a central European background site (Melpitz, Germany) in winter, *Atmospheric Chemistry and Physics* **21**, 635–655 (2021).